257 (2026) 214246

Contents lists available at ScienceDirect

Geoenergy Science and Engineering

journal homepage: www.sciencedirect.com/journal/geoenergy-science-and-engineering

High-Fidelity saturation prediction using physics-informed attention neural network

Yinhong Tian [a,b,*], Guiwen Wang [a,b,**], Hongbin Li [a,b], Jin Lai [a,b]

[a] State Key Laboratory of Petroleum Resources and Engineering, China University of Petroleum (Beijing), Beijing, 102249, China
[b] College of Geosciences, China University of Petroleum (Beijing), Beijing, 102249, China

ARTICLE INFO

Keywords:
Water saturation prediction
Ultradeep tight sandstone reservoirs
Physics-informed neural network (PINN)
Deep learning
Window and axial attention mechanisms

ABSTRACT

Accurate estimation of water saturation is critical for reservoir characterization and optimal production strategies in ultra-deep tight sandstone gas reservoirs. However, traditional empirical models often fail to provide reliable predictions due to the inherent heterogeneity and nonlinear interactions within these reservoirs. To address these challenges, this paper proposes the Saturation Neural Network (SatuNN), a novel deep learning framework that combines CNNs, window attention, axial attention and BiLSTM to capture multi-scale spatio-temporal features from logging data. Specifically, the CNNs and window attention layers capture local spatial features, while the BiLSTM and axial attention layers address global temporal dependencies. The proposed model leverages a physics-informed neural network strategy to embed petrophysical constraints directly into the training process, ensuring physically consistent and geologically meaningful predictions. Comprehensive evaluations using core and logging data from ultradeep tight sandstone reservoirs in the Tuha Basin demonstrate that SatuNN achieves superior predictive accuracy and significantly lower errors (R^2 = 0.92, MAE = 3.27 %) compared to both the optimal ablation baseline model (Without WA: R^2 = 0.86, MAE = 4.51 %) and traditional petrophysical model (Archie: R^2 = 0.84, MAE = 4.83 %). Moreover, successful field applications in two blind-test wells further validate the robustness and practical applicability of the proposed model. The presented SatuNN framework provides an accurate approach for saturation prediction in ultradeep tight sandstone gas reservoirs, effectively offering potential to improve reservoir evaluation and field development strategies.

1. Introduction

Water saturation (Sw) represents a fundamental petrophysical parameter critical for hydrocarbon reserve estimation and reservoir characterization (Xu et al., 2017; Zhang et al., 2022). Precise Sw determination significantly impacts production strategy optimization and economic assessment of hydrocarbon fields (Tatar et al., 2014; Miah et al., 2020). However, saturation quantification remains challenging due to the complex interplay of multiple reservoir factors, including diagenesis (Zhou et al., 2019), lithofacies variation (Ren et al., 2022), and pore structure heterogeneity (Fan et al., 2019). These interactions manifest as pronounced nonlinear relationships among reservoir parameters, complicating accurate Sw calculation. While core analysis via laboratory testing provides the most direct and reliable Sw measurements, this approach faces substantial limitations in practical oilfield operations (Al-Bulushi et al., 2009; Baziar et al., 2016). The prohibitive costs, operational complexities, and time constraints associated with core sampling preclude comprehensive measurements across all wells, necessitating alternative methodologies for widespread Sw determination in reservoir characterization workflows.

To acquire reservoir saturation data, researchers have explored diverse methodologies (Jafari Kenari and Mashohor, 2013; Amiri et al., 2015; Xiao et al., 2021). The most cost-effective approach leverages conventional logging data to estimate saturation (Shahin et al., 2012), leading to three primary categories of methods. The first category employs empirical or semi-empirical fitting formulas—both linear and nonlinear—that relate reservoir parameters, such as porosity (Movahhed et al., 2019), to water saturation. However, these simplified models frequently fail to achieve requisite prediction accuracy due to their inability to capture complex reservoir heterogeneities. The second category centers on petrophysical modeling. This approach is grounded in analyzing reservoir conduction mechanisms and developing

* Corresponding author. State Key Laboratory of Petroleum Resources and Engineering, China University of Petroleum (Beijing), Beijing, 102249, China
** Corresponding author. State Key Laboratory of Petroleum Resources and Engineering, China University of Petroleum (Beijing), Beijing, 102249, China
E-mail addresses: cupbtyh@163.com (Y. Tian), wanggw@cup.edu.cn (G. Wang).

https://doi.org/10.1016/j.geoen.2025.214246
Received 21 May 2025; Received in revised form 4 August 2025; Accepted 5 October 2025
Available online 9 October 2025

petrophysical models that relate Sw to measurable logging responses. Archie's seminal work (Archie, 1942) derived a foundational model for clean sandstones, relating Sw to electrical conductivity, and has seen widespread application. Nevertheless, many reservoirs, particularly unconventional formations, exhibit significant deviations from Archie behavior ('non-Archie') due to complex conduction phenomena such as mixed wettability (Afrapoli et al., 2009), clay mineral conductivity (Xing et al., 2023), and fracture networks (Sun et al., 2021). To address Sw estimation in these heterogeneous settings, subsequent research has focused on developing increasingly sophisticated petrophysical models and nonlinear response equations (Mashaba and Altermann, 2015; Zhang and Xu, 2016). Models like Simandoux (1963), Indonesian (Poupon and Leveaux, 1971), and Dual-Water (Clavier et al., 1984) incorporate additional parameters to account for reservoir heterogeneity, effectively attempting to map a multidimensional parameter space to Sw. While these advanced petrophysical models strive to encompass a broader range of reservoir parameters, their inherent reliance on simplified representations of complex physical processes and empirical parameter fitting can still limit their predictive accuracy, especially in highly complex geological scenarios. The third category leverages deep learning (DL) methodologies, driven by the increasing availability of geoscientific data and the remarkable advancements in DL across diverse domains (Bergen et al., 2019). DL techniques offer powerful tools for establishing complex, data-driven mappings between high-dimensional input features and target variables. Consequently, geoscientists have increasingly explored DL for tackling various subsurface challenges. Deep learning has been successfully applied to reservoir characterization tasks including reservoir parameter prediction (Chen et al., 2020; Ameur-Zaimeche et al., 2022), lithology classification (Zhang et al., 2021; Zheng et al., 2021b) and seismic data processing (Liu et al., 2022a; Dong et al., 2022). Current DL architectures predominantly applied in geoscience include Fully Connected Networks (FCNs) (Zheng et al., 2021a), Convolutional Neural Networks (CNNs) (de Lima et al., 2020), and Recurrent Neural Networks (RNNs) (Jiang et al., 2020).

Analysis of the aforementioned saturation prediction methodologies reveals two fundamental approaches for calculating water saturation from logging data: model-based methods and data-driven methods. Model-based approaches characterize the conduction mechanisms within heterogeneous porous media through mathematical formulations, including the Archie formula, Waxman-Smits model, dual-water model, and conductive rock matrix model. These petrophysical frameworks are grounded in established physical principles—Ohm's law, Darcy's law, and electrochemical laws—and are expressed as complex nonlinear equations with multiple unknown parameters. Several researchers have advanced these model-based approaches. Amiri et al. (2012) enhanced the conventional Indonesian model through semi-empirical equations incorporating resistivity, gamma ray, neutron, and density logging responses, with validation across multiple tight sandstone gas reservoirs. Su et al. (2020) formulated a stress-sensitive saturation calculation model based on capillary pressure relationships and fractal theory. Oraby (2021) developed a non-Archie saturation framework specifically addressing carbonate reservoir heterogeneities, achieving robust prediction results validated against core measurements. Despite their predictive accuracy, these models often encounter computational challenges due to their complexity and the large number of variables involved, which can limit their practical applicability in rapid evaluations.

Data-driven methods leverage the robust nonlinear mapping capabilities of machine learning algorithms to establish direct relationships between input logging parameters and saturation values, without explicit consideration of underlying physical mechanisms (Zhong et al., 2019). These approaches have gained significant traction in reservoir characterization and saturation prediction (Yang et al., 2022a; Bai et al., 2022b; Liu et al., 2023). Weinzierl and Wiese (2021) employed deep learning techniques to extract petrophysical properties and constructed a comprehensive saturation prediction model incorporating fluid migration dynamics. Wei et al. (2022) developed a methodology utilizing two-dimensional reservoir pressure fields derived from geological and production data as inputs to Convolutional Long Short-Term Memory (ConvLSTM) networks, enabling high-dimensional feature extraction for predicting hydrocarbon and water saturation distributions with commendable accuracy and computational efficiency. Lin et al. (2023) leveraged the inductive bias advantages of Convolutional Neural Networks (CNNs) to extract multi-scale reservoir features from logging data, facilitating precise saturation prediction in complex carbonate reservoirs. Hu et al. (2024) proposed a water saturation prediction framework based on Gated Recurrent Unit (GRUs) networks, trained and validated using extensive conventional petrophysical datasets. Despite their promising applications, data-driven methodologies face specific limitations in geoscience implementations. Constructing high-performance deep learning architectures capable of capturing temporal dependencies and spatial patterns within geological structures often necessitates complex multi-level networks (Afrasiabi et al., 2021). These sophisticated architectures may encounter challenges including overfitting, training instability, or convergence issues, potentially compromising model generalization capabilities and prediction performance (Li et al., 2021). Furthermore, data quantity and quality significantly impact model efficacy, particularly in geological settings characterized by data scarcity or heterogeneity, where models may struggle to adequately characterize complex geological features (Wu et al., 2018). These challenges underscore the need for further research into robust training techniques and strategies to improve the generalization and reliability of data-driven models in geological applications.

Physics-Informed Neural Network (PINN) provide an innovative framework for integrating the respective advantages of model-based and data-driven approaches (Raissi et al., 2019; Chen et al., 2024; Latrach et al., 2024; Wang et al., 2024b). In recent years, PINN have achieved significant advances in geoscience, with successful applications in seismic full waveform inversion (Song and Alkhalifah, 2022; Muller et al., 2023; Zhang et al., 2023a), fluid simulation and prediction in porous media (Almajid and Abu-Al-Saud, 2022; Zhang et al., 2023b) and parameter inversion for unconventional reservoirs (Li et al., 2024; Chakraborty et al., 2025). PINN typically incorporate physical constraints into deep learning models by embedding three types of bias: observational bias, learning bias and inductive bias (Karniadakis et al., 2021). Lv et al. (2021) generated synthetic training data by numerically solving the Navier-Stokes and elastic wave equations on fractured coal models, subsequently coupling these physics-based datasets with laboratory measurements to train a deep neural network (DNN). This methodology realized a PINN framework without directly invoking physical equation residuals during network training. Zheng et al. (2023) implemented a weak-form PINN by initially training a neural network to simulate seismic responses from P-wave velocity and density inputs, and then embedding these network-generated outputs as physics-based constraints within the loss function of a CNN-BiLSTM architecture. These studies introduced observational bias by employing synthetic training data closely reflecting underlying physical processes or carefully designed data-augmentation schemes, thereby guiding the model towards greater physical consistency. In contrast, Xiong et al. (2021) trained a DNN to predict elastic coefficients derived from Biot theory using logging data, embedding theoretical priors into the loss function combining data misfit terms with physical inequality constraints. This approach enabled precise regression of key shale-oil reservoir parameters. Similarly, Wang et al. (2024a) developed a PINN integrating Caputo fractional derivatives and automatic differentiation into the loss function, supplemented by sparse regression to infer fractional-order differential equations governing shale gas production decline. Their approach yielded accurate and interpretable production forecasts, emphasizing the value of explicitly embedding physical laws within network training. These examples demonstrate the application of learning bias by explicitly adding penalty terms, such as physical

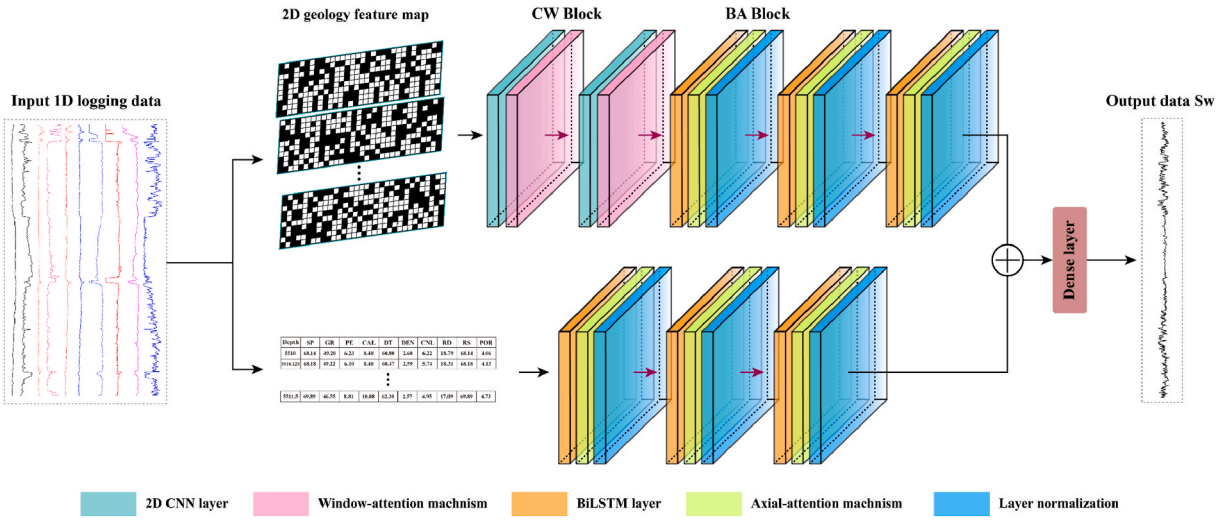

Fig. 1. Architecture of the proposed Saturation Neural Network (SatuNN). The model adopts a dual-branch architecture consisting of Convolutional-Window attention (CW) Blocks and BiLSTM–Axial attention (BA) Blocks to capture multiscale features from logging data. In the upper branch, two CW Blocks and three BA Blocks process two-dimensional geological feature maps transformed from one-dimensional logging curves, enabling extraction of both spatial and temporal characteristics. The lower branch employs three BA Blocks to preserve and enhance inherent temporal patterns from the original one-dimensional data. Both feature pathways are subsequently fused through a Feature Concatenation strategy before passing through fully connected layers for final saturation predictions.

equation residuals or inequality constraints, into loss functions, ensuring adherence to underlying physical laws while fitting observational data. Additionally, the strategy of incorporating learning bias through geological constraints in the loss function, as well as inductive bias via embedding physical priors within specialized network architectures, has also demonstrated widespread advantages in various inversion tasks. For instance, Lu et al. (2024) designed a physics-informed recurrent neural network (PIRNN) for elastic FWI of vertical seismic profiling (VSP) data by encoding geological knowledge, wellbore velocity knowledge, and empirical relationships into the loss function via regularization terms, while the RNN architecture itself is constrained by the elastic wave equation, thereby significantly enhancing inversion accuracy and convergence efficiency and showing preliminary robustness against moderate Gaussian noise. Overall, PINNs provide a powerful framework that exploits the nonlinear modeling capabilities of deep learning while embedding physical equations, such as PDEs or the numerous nonlinear algebraic equations in petrophysics, as prior knowledge into model, thereby enhancing the physical consistency of the trained model and significantly improving their applicability to specific tasks.

Building upon these developments in PINN, we propose a novel approach that synergistically integrates the respective advantages of data-driven and petrophysical methodologies. Our approach establishes high-dimensional nonlinear spatial mapping relationships between logging data and reservoir parameters by integrating complementary deep learning modules, including feature extraction (CNNs), temporal correlation (RNNs), and global attention mechanisms. Concurrently, we incorporate geological prior information derived from established petrophysical models, thereby constructing an end-to-end reservoir saturation prediction framework designated as the Saturation Neural Network (SatuNN). The proposed architecture comprises two two-dimensional CNNs layers, three bidirectional long short-term memory (BiLSTM) layers, and two distinct attention mechanisms (window attention and axial attention). We rigorously evaluated our model's performance against both traditional petrophysical methodologies and state-of-the-art deep learning architectures. Furthermore, we conducted ablation studies by systematically modifying the internal components of SatuNN to assess the contribution of each architectural element to overall model performance. The principal contributions of this research are summarized as follows.

1) We propose an innovative hybrid architecture combining CNN layer with window attention mechanism (CW Block) and BiLSTM layer with axial attention mechanism (BA Block) to effectively capture multi-scale spatiotemporal features embedded within logging data.
2) We establish a comprehensive multivariate conductive petrophysical saturation model, incorporating effective medium theory and the Hanai-Bruggeman model, which is seamlessly integrated into the SatuNN framework through the PINN methodology. This integration imposes physical constraints that facilitate efficient convergence, enhance model generalization capabilities, and improve consistency with underlying physical mechanisms.
3) We validate the SatuNN model for saturation prediction in deep tight sandstone reservoirs and demonstrate its superior performance compared to both traditional petrophysical models and state-of-the-art deep learning approaches. Furthermore, our comparative analyses of model variants, which were constructed by modifying the internal components of SatuNN, underscore the effectiveness of the proposed architecture.

The remainder of this paper is organized as follows. Section 2 details the proposed methodology, including the model architecture and loss function formulations. Section 3 describes the data preprocessing and model training. Section 4 presents experimental results and discussion. Finally, Section 5 concludes the paper.

2. Methodology

2.1. Overall architecture

The proposed Saturation Neural Network (SatuNN) employs a parallel architecture comprising multiple Convolutional-Window attention (CW) Blocks and BiLSTM-Axial attention (BA) Blocks to extract multi-scale features from logging data, as illustrated in Fig. 1. This dual-branch structure enables comprehensive feature extraction, with the upper branch consisting of two CW Blocks and three BA Blocks, while the lower branch comprises three BA Blocks. The synergistic integration of feature engineering and model structural characteristics forms the foundation for the network's exceptional performance. For data preprocessing, we adopt the methodology proposed in Tian et al. (2024), transforming one-dimensional logging curves into two-dimensional geological feature maps, as detailed in Section 3.2. These transformed representations

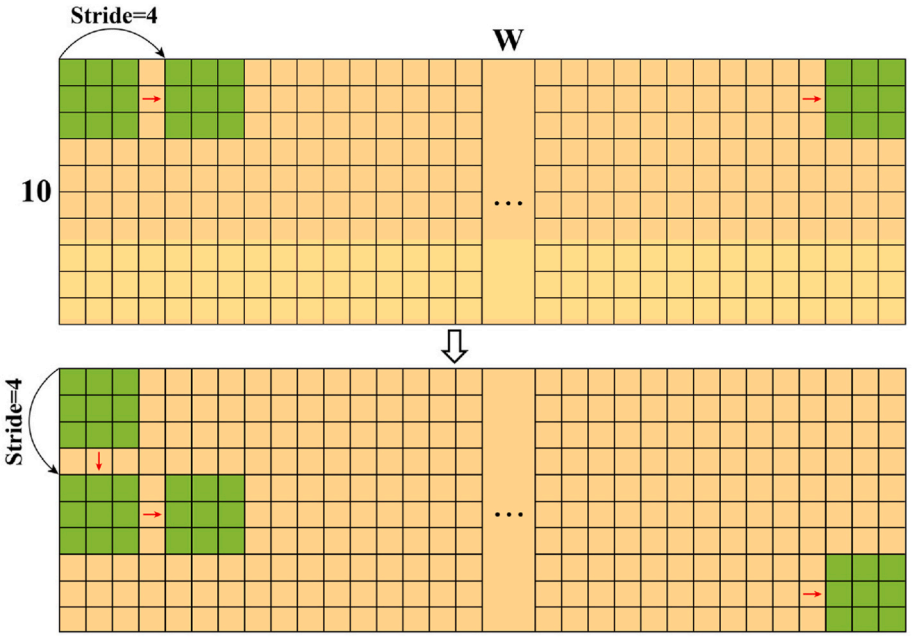

Fig. 2. Schematic illustration of the window attention mechanism within the CW Block. The upper panel depicts horizontal sliding operations across two-dimensional geological feature maps with a window size of 3 (green grids) and a horizontal stride of 4, effectively highlighting local feature extraction along the depth direction (W). The lower panel similarly illustrates vertical sliding operations along the logging-curve direction (10 input logging channels) using the same window size and stride, emphasizing the extraction of spatial correlations across different logging parameters. (For interpretation of the references to colour in this figure legend, the reader is referred to the Web version of this article.)

serve as input to the upper branch, where CW Blocks and BA Blocks synergistically extract spatiotemporal features through the combined advantages of two-dimensional convolutional neural networks and bidirectional long short-term memory networks. Concurrently, to preserve information integrity, the original one-dimensional logging data is processed through the lower branch's BA Blocks to extract inherent temporal features. This parallel structure mitigates potential information loss during data transformation, enabling effective feature fusion by simultaneously processing the transformed two-dimensional data while leveraging original features extracted by the auxiliary pathway.

The network processing flow begins with normalization of logging data to ensure scale consistency across input parameters. Subsequently, the normalized data traverses two parallel feature extraction pathways for multi-scale feature learning: 1) The first pathway transforms one-dimensional logging data into two-dimensional representations through a specialized high-dimensional mapping strategy. These transformations undergo feature extraction via two CW Blocks composed of two-dimensional convolutional neural networks and window attention mechanisms, capturing spatial features and local information. The resulting representations are further processed through three BA Blocks comprising bidirectional long short-term memory networks, axial attention mechanisms, and normalization layers to extract sequential features and enhance contextual understanding. 2) The second pathway directly processes the normalized logging curves through three BA Blocks, preserving and enhancing the inherent temporal patterns in the original data while ensuring information integrity (Fig. 1). Layer normalization is strategically integrated within each BA Block to mitigate internal covariate shift during training iterations and accelerate convergence. The high-dimensional feature vectors from both pathways undergo fusion through a Feature Concatenation strategy before being processed by fully connected layers to generate the final saturation predictions. This meticulously designed architecture transcends the limitations of conventional methods for saturation prediction from logging data, providing more accurate and robust estimation of reservoir parameters through the comprehensive integration of spatial and temporal features at multiple scales.

2.2. D2-CNN with window attention block (CW Block)

Two-dimensional convolutional neural networks (2D CNNs) have emerged as one of the most widely adopted deep learning architectures in geoscience (Yang et al., 2021; Liu et al., 2021a), owing to their powerful feature extraction capabilities and computational efficiency. Their convolution operations, based on local receptive fields and weight sharing, can substantially reduce model complexity while preserving the ability to capture spatial features (Li et al., 2021; He et al., 2016). In this work, the input $X \in \mathbb{R}^{10\times W\times 1}$ denotes two-dimensional image data transformed from 10 logging curves, where 1 represents the number of channels. The convolution operation using a two-dimensional convolutional layer with a kernel size of $f \times f$ on X can be mathematically expressed as:

$$Y = ReLU\left(\sum_{m=0}^{f-1}\sum_{n=0}^{f-1} X_{i+m,j+n} * W_{m,n} + b_{m,n}\right) \tag{1}$$

where $Y \in \mathbb{R}^{10\times W\times C}$ represents high-dimensional features output by the two-dimensional convolutional layer, * denotes the convolution operation, $W_{m,n}$ and $b_{m,n}$ are the network's trainable parameters, and $ReLU$ is the nonlinear activation function frequently employed in deep learning. After extracting high-dimensional features via the two-dimensional convolutional layer, a window attention layer (Liu et al., 2021b) is introduced to dynamically adjust feature weights within local regions, thereby capturing salient information in the input data more effectively. The window attention mechanism is analogous to convolution with a stride of 1, where the window size corresponds to the convolution kernel. However, convolution only learns a single set of projection parameters, whereas the attention mechanism learns projection matrices Q, K, and V to quantify correlations among points within the window. Suppose the window operates with size $WS = 3$ on the input $Y \in \mathbb{R}^{10\times W\times C}$ for one channel, as illustrated in Fig. 2. The window then slides over the input data with stride $S = 4$, computing attention for each window:

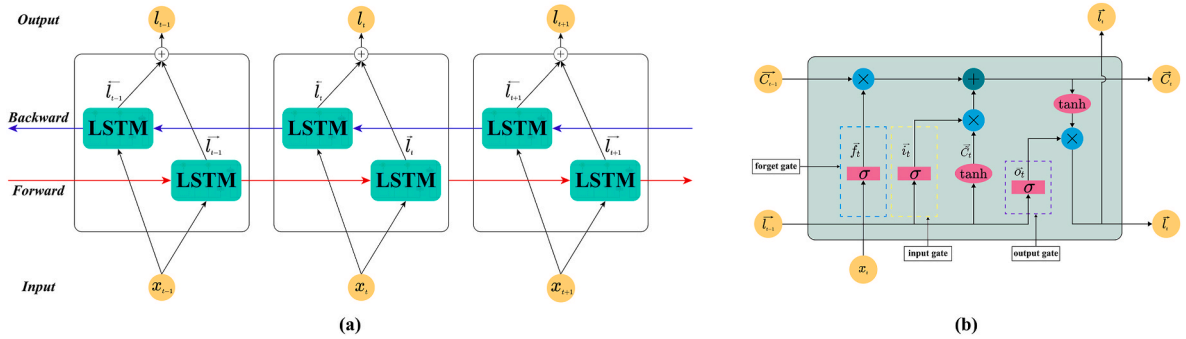

Fig. 3. Structural overview of the bidirectional long short-term memory network (BiLSTM). (a) Conceptual diagram highlighting forward and backward computations to integrate past and future sequence information. (b) Detailed schematic of the internal structure, illustrating the operational flow of forget, input, and output gates within a single LSTM cell.

$$SA\left(W_k^Q Y_i, W_k^K Y_i, W_k^V Y_i\right) = softmax\left(\frac{Q_k^i \left(K_k^i\right)^T}{\sqrt{d_k}} + B\right) V_k^i \tag{2}$$

where W_k^Q, W_k^K and W_k^V are trainable parameter matrices that project the input into k attention heads Q_k, K_k and V_k, Y_i represents the input data in the *i-th* window, d_k is Q_k/K_k, and B is the relative position bias. By integrating two-dimensional convolutional neural networks with window attention mechanisms, CW Block effectively focuses on critical regions within input features, adaptively adjusting feature weights within localized areas to capture essential information and enhance the model's capacity to characterize complex patterns in logging data.

2.3. BiLSTM with axial attention block (BA Block)

The BA Block integrates Bidirectional Long Short-Term Memory (BiLSTM) layers with an axial attention mechanism to capture both long-term dependencies and global contextual information in sequential data. BiLSTM extends the standard LSTM architecture by processing the input sequence in both forward and backward directions, allowing it to incorporate past and future states when computing hidden representations (Yang et al., 2022b). By combining hidden states from these two directions at each time step, BiLSTM offers improved performance for tasks such as natural language processing and time series prediction (dos Santos et al., 2021; Kim et al., 2023). The primary distinction between BiLSTM and traditional LSTM lies in the final output, which is formed by concatenating the forward and backward outputs at each time step, as illustrated in Fig. 3. The primary difference lies in how the current outputs are derived: in forward computation, the current output $\overrightarrow{l_t}$ depends on the output $\overrightarrow{l_{t-1}}$ at the previous time step $t-1$, while in backward computation, the current output $\overleftarrow{l_t}$ depends on the output $\overleftarrow{l_{t+1}}$ at the next time step $t+1$. In SatuNN, once the CW Block has completed its operations, its output is fed into the BiLSTM's forget gate f_t. The forget gate is the first gate in an LSTM and determines which information should be discarded from the previous cell state $C_{t-1}(C_{t+1})$, as shown in Eq. (3):

$$\begin{aligned} \overrightarrow{f_t} &= \sigma\left(\overrightarrow{W_f} \cdot \left[\overrightarrow{l_{t-1}}, x_t\right] + \overrightarrow{b_f}\right) \\ \overleftarrow{f_t} &= \sigma\left(\overleftarrow{W_f} \cdot \left[\overleftarrow{l_{t+1}}, x_t\right] + \overleftarrow{b_f}\right) \end{aligned} \tag{3}$$

where $\overrightarrow{l_{t-1}}$ and $\overleftarrow{l_{t+1}}$ represent the hidden states of the previous cell unit at time step t for forward and backward calculations, x_t is the input data at time t, $\overrightarrow{W_f}$ and $\overleftarrow{W_f}$ represent the weight matrices of the forget gate in forward and backward computations, $\overrightarrow{b_f}$ and $\overleftarrow{b_f}$ represent the corresponding bias terms, and σ is the sigmoid activation, which restricts outputs to the range [0,1]. The second gate is the input gate i_t, which determines the information to be added to the candidate cell state at current time step t, as shown in Eq. (4):

$$\begin{aligned} \overrightarrow{i_t} &= \sigma\left(\overrightarrow{W_i} \cdot \left[\overrightarrow{l_{t-1}}, x_t\right] + \overrightarrow{b_i}\right) \\ \overleftarrow{i_t} &= \sigma\left(\overleftarrow{W_i} \cdot \left[\overleftarrow{l_{t+1}}, x_t\right] + \overleftarrow{b_i}\right) \end{aligned} \tag{4}$$

where $\overrightarrow{W_i}$ and $\overleftarrow{W_i}$ are the weight matrices for forward and backward computations, and $\overrightarrow{b_i}$ and $\overleftarrow{b_i}$ are the corresponding bias terms. The third step involves updating the new candidate cell state $\overrightarrow{\widetilde{C}_t}\left(\overleftarrow{\widetilde{C}_t}\right)$ based on the input of the current time step, and updating the new cell state $\overrightarrow{C_t}\left(\overleftarrow{C_t}\right)$ by combining the outputs of the forget, the input gates and the cell state from the previous time step $\overrightarrow{C_{t-1}}\left(\overleftarrow{C_{t+1}}\right)$, as shown in Eqs. (5) and (6):

$$\begin{aligned} \overrightarrow{\widetilde{C}_t} &= \varphi\left(\overrightarrow{W_{\tilde{C}}} \cdot \left[\overrightarrow{l_{t-1}}, x_t\right] + \overrightarrow{b_{\tilde{C}}}\right) \\ \overleftarrow{\widetilde{C}_t} &= \varphi\left(\overleftarrow{W_{\tilde{C}}} \cdot \left[\overleftarrow{l_{t+1}}, x_t\right] + \overleftarrow{b_{\tilde{C}}}\right) \end{aligned} \tag{5}$$

$$\begin{aligned} \overrightarrow{C_t} &= \overrightarrow{f_t} \odot \overrightarrow{C_{t-1}} + \overrightarrow{i_t} \odot \overrightarrow{\widetilde{C}_t} \\ \overleftarrow{C_t} &= \overleftarrow{f_t} \odot \overleftarrow{C_{t+1}} + \overleftarrow{i_t} \odot \overleftarrow{\widetilde{C}_t} \end{aligned} \tag{6}$$

where $\overrightarrow{W_{\tilde{C}}}$ and $\overleftarrow{W_{\tilde{C}}}$ denote the weight matrices for forward and backward computations, $\overrightarrow{b_{\tilde{C}}}$ and $\overleftarrow{b_{\tilde{C}}}$ are the corresponding bias terms, φ is the tanh function, and $\odot$ represents element-wise multiplication. The last gate is the output gate O_t, and the output of BiLSTM l_t is calculated through the output gate and the updated cell state from the previous time step, as shown in Eqs. (7)–(9):

$$\begin{aligned} \overrightarrow{O_t} &= \sigma\left(\overrightarrow{W_O} \cdot \left[\overrightarrow{l_{t-1}}, x_t\right] + \overrightarrow{b_O}\right) \\ \overleftarrow{O_t} &= \sigma\left(\overleftarrow{W_O} \cdot \left[\overleftarrow{l_{t+1}}, x_t\right] + \overleftarrow{b_O}\right) \end{aligned} \tag{7}$$

$$\begin{aligned} \overrightarrow{l_t} &= \overrightarrow{O_t} \cdot \varphi\left(\overrightarrow{C_t}\right) \\ \overleftarrow{l_t} &= \overleftarrow{O_t} \cdot \varphi\left(\overleftarrow{C_t}\right) \end{aligned} \tag{8}$$

$$l_t = \overrightarrow{l_t} \bigoplus \overleftarrow{l_t} \tag{9}$$

where $\overrightarrow{W_O}$ and $\overleftarrow{W_O}$ represent the weight matrices of the output gate for forward and backward computations, $\overrightarrow{b_O}$ and $\overleftarrow{b_O}$ are the corresponding bias terms, and $\bigoplus$ denotes concatenation of the forward and backward outputs to form the final BiLSTM output.

The axial attention mechanism (Ho et al., 2019) addresses the computational limitations of conventional attention methods while retaining long-range global information. It processes high-dimensional axial attention and width axial attention in parallel by exchanging

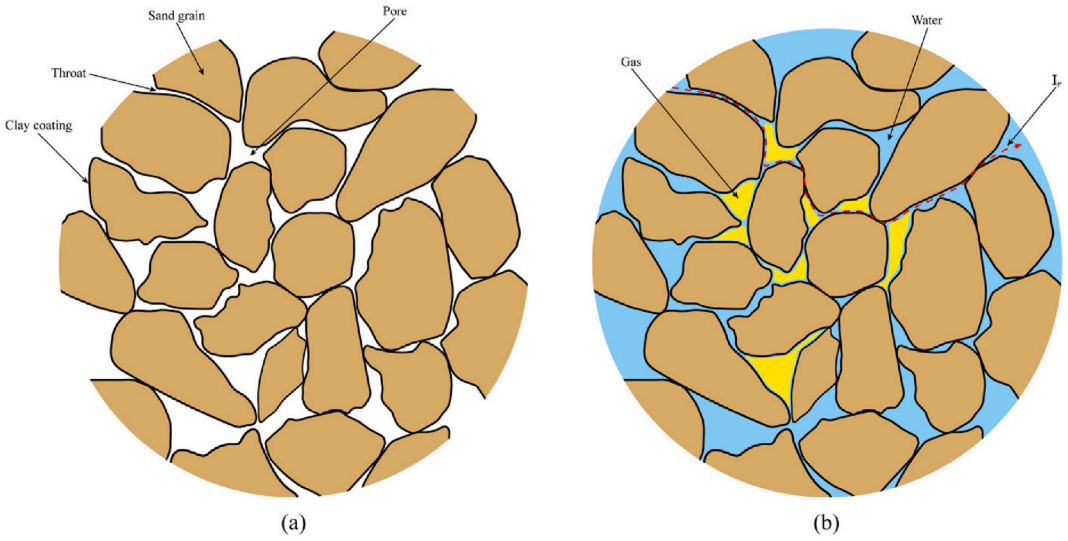

Fig. 4. Schematic illustration of the petrophysical multiphase conductive model for ultra-deep tight sandstone reservoirs. (a) Microscale pore structure illustrating the grain arrangement, pore spaces, and clay mineral coating surrounding grain surfaces. (b) Illustration of multiphase fluid distribution and conductivity pathways within tight sandstone pores. The current (I_r) is conducted along the grain surfaces and pore water (blue regions), while the pore spaces filled with hydrocarbons (yellow regions) act as insulators. (For interpretation of the references to colour in this figure legend, the reader is referred to the Web version of this article.)

information across different axes to achieve global attention (Liu et al., 2022b; Wu et al., 2024). For axial attention, the BiLSTM output $l \in \mathbb{R}^{N\times L\times H}$ is divided into non-overlapping high-dimensional axial attention sequences and width axial attention sequences:

$$l^h = \left[l_1^h, l_2^h, \cdots, l_N^h\right]$$
$$l^v = \left[l_1^v, l_2^v, \cdots, l_L^v\right]$$

where l_i^h and l_i^v represent high-dimensional and width axial attention feature vectors, and H is the number of input channels. Next, Multi-Head Self-Attention (MHSA) is applied to each divided sequence. Each sequence is first split into k heads, and self-attention is computed for each head, as shown in Eqs. (10)–(12):

$$\begin{aligned}\left(Y_k^h\right)^i &= SA\left(W_k^Q l_i^h, W_k^K l_i^h, W_k^V l_i^h\right)\\ \left(Y_k^v\right)^i &= SA\left(W_k^Q l_i^v, W_k^K l_i^v, W_k^V l_i^v\right)\end{aligned} \tag{10}$$

$$\begin{aligned}Y_k^h &= \left[\left(Y_k^h\right)^1, \left(Y_k^h\right)^2, \cdots, \left(Y_k^h\right)^N\right]\\ Y_k^v &= \left[\left(Y_k^v\right)^1, \left(Y_k^v\right)^2, \cdots, \left(Y_k^v\right)^L\right]\end{aligned} \tag{11}$$

$$\begin{aligned}Y^h &= Concat\left(Y_1^h, \cdots, Y_k^h\right)\\ Y^v &= Concat\left(Y_1^v, \cdots, Y_k^v\right)\end{aligned} \tag{12}$$

where $SA(\cdot)$ denotes the multi-head self-attention function (consistent with Eq. (2)), and W_k^Q, W_k^K, W_k^V are trainable parameter matrices that project the input to obtain query, keys, and value for k heads. Consequently, the outputs Y_k^h and Y_k^v are the results of the multi-head attention mechanism for the k-*th* head. Axial-Attention enhances the interaction between features and the global context modeling. Thus, BA Block enhances the model's understanding and processing capabilities for sequential data, enabling it to capture global information for specific well data and correlation information between different well data.

2.4. Petrophysics model and loss function

Ultradeep tight sandstone reservoirs present considerable challenges for reservoir evaluation due to their complex pore structures and pronounced heterogeneity (Zhang et al., 2024; Jin et al., 2024). These reservoirs exhibit ultra-low porosity and permeability, and their electrical conduction mechanisms are substantially more complex than those of conventional reservoirs (Liu et al., 2015). At the microscopic scale, tight sandstones typically contain a complicated pore network system that includes primary pores, secondary dissolution pores, and microfractures, as well as high, unevenly distributed clay content (Zhao et al., 2015; Wang et al., 2020). This combination forms a distinctive "matrix–pore–clay" multicomponent conductive system (Fig. 4). The multiple conduction pathways in these reservoirs can result in substantial errors when applying the traditional model. Therefore, following the approach of Gupta and Kamal (2023), we begin by examining the microscopic conduction mechanisms and incorporating effective medium theory (Bussian, 1983) and mixing theory (Glover, 2010) to construct a petrophysical model that captures the characteristics of the target reservoir. In this model, the sandstone grains are assumed to be non-conductive cores with a uniformly distributed clay coating on their surfaces (Fig. 4). This clay coating allows current flow along the grain surfaces, forming conductive particles. As a result, the overall rock conductivity depends on both the formation water conductivity and the grain conductivity. More specifically, the matrix grains and the pore fluid can be conceptualized as two interlocking lattice-like structures: contacts among matrix grains form one lattice, while the fluid in the pore space forms another. Based on effective medium theory, the conductivity of a system composed of two such interlocking structures can be described by the Hanai-Bruggeman (HB) equation (Bruggman, 1935; Hanai et al., 1959):

$$\sigma_t = \sigma_f \phi^{m_e}\left(\frac{1-\sigma_s/\sigma_f}{1-\sigma_s/\sigma_t}\right)^{m_e} \tag{13}$$

where σ_s is the conductivity of the matrix grains, σ_f is the conductivity of the pore fluid, and m_e is the cementation exponent used when modeling the actual conductivity with effective medium theory.

To calculate the multiphase fluid conductivity σ_f in Eq. (13), we employ mixing theory. According to the general mixing rule (Glover, 2010), any physical property P of a mixture consisting of n components can be expressed as:

$$P = \left[\sum_{i=1}^{n} V_i P_i^M\right]^{1/M} \tag{14}$$

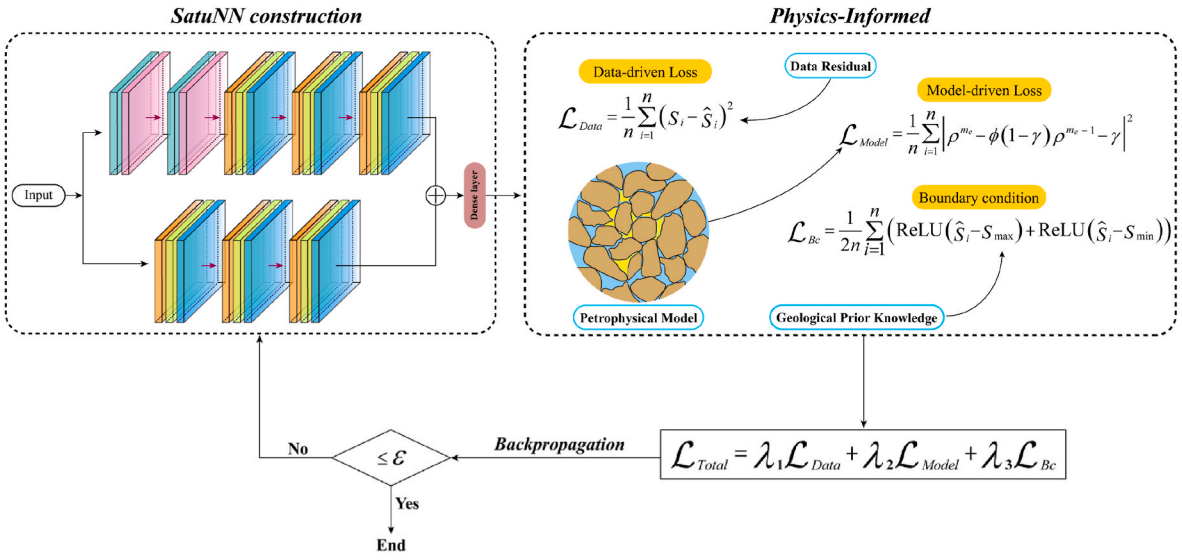

Fig. 5. Framework of physics-informed neural network training and optimization strategy utilized by the proposed SatuNN model. The left box depicts the dual-branch SatuNN model architecture. The right box elaborates on the physics-informed training process, incorporating three specialized loss functions: data-driven loss ($\mathscr{L}_{Data}$), model-driven petrophysical loss ($\mathscr{L}_{Model}$), and boundary-condition loss ($\mathscr{L}_{Bc}$). These loss terms are integrated to form the total loss function ($\mathscr{L}_{Total}$), ensuring that network predictions consistently satisfy geological and petrophysical constraints.

if the value of this property for the *i-th* component is P_i, and its volume fraction is V_i. In this expression, M is known as the mixing coefficient and ranges from $[-1,1]$. When $M = 1$, the components are arranged in parallel, and when $M = -1$, they are arranged in series. In our scenario, the pore fluid is considered a binary mixture of formation water and hydrocarbons (Fig. 4(b)). According to Eq. (14), its conductivity can be expressed as:

$$\sigma_f = \left[S_W \sigma_W^{n_m} + (1 - S_W)\sigma_h^{n_m}\right]^{1/n_m} \tag{15}$$

where S_W is the water saturation, $1 - S_W$ is the hydrocarbon saturation, σ_h is the hydrocarbons conductivity, and n_m is the mixing coefficient corresponding to the saturation exponent in fluid conductivity calculations. The hydrocarbon resistivity is typically very high, meaning $\sigma_h \approx 0$. Substituting this approximation into Eq. (15) yields:

$$\sigma_f = \sigma_W S_W^{1/n_m} \tag{16}$$

Finally, combining Eqs. (13)–(16) produces the following petrophysical model:

$$\sigma_t = \sigma_W S_W^{1/n_m} \phi^{m_e} \left(\frac{1 - \sigma_s \Big/ \left(\sigma_W S_W^{1/n_m}\right)}{1 - \sigma_s/\sigma_t} \right)^{m_e} \tag{17}$$

Having established this petrophysical model, our objective is to integrate its prior knowledge into the training of the SatuNN model via a physics-informed neural network (PINN). Fig. 5 shows the training process of SatuNN and its associated loss function. By embedding constraint terms derived from the petrophysical equations into the loss function, the deep learning model can capture both data-driven statistical features and the underlying physical principles of the target reservoir. This physics-guided deep learning strategy merges the strengths of data-driven and model-driven methods, ensuring physically plausible predictions while harnessing deep learning's capability to handle complex nonlinear relationships (Zhang et al., 2023a). Note that Eq. (17) is an implicit function, making it difficult to solve directly. In Fig. 5, it has been reformulated into a solvable expression:

$$\begin{aligned} &\rho^{m_e} - \phi(1-\gamma)\rho^{m_e - 1} - \gamma = 0 \\ &\rho = \left(\frac{\sigma_t}{\sigma_f}\right)^{1/m_e} \quad \gamma = \frac{\sigma_s}{\sigma_f} \end{aligned} \tag{18}$$

The optimization objective of SatuNN is to minimize the error between the predicted and true saturation values. From the data-driven perspective, we employ the mean squared error (MSE) loss, which emphasizes larger errors, making it suitable for our application:

$$\mathscr{L}_{Data} = \frac{1}{n} \sum_{i=1}^{n} (S_i - \widehat{S}_i)^2 \tag{19}$$

where n is the number of training samples, S_i and $\widehat{S}_i$ denote the true and predicted saturation values, respectively. The model-driven loss function is expressed as:

$$\mathscr{L}_{Model} = \frac{1}{n} \sum_{i=1}^{n} \left| \rho^{m_e} - \phi(1-\gamma)\rho^{m_e - 1} - \gamma \right|^2 \tag{20}$$

Due to the influences of depositional environments, structural settings, and other factors, a specific reservoir typically exhibits unique geological features and reservoir properties (Bai et al., 2022a). The reservoir investigated in this study is a high water-cut reservoir, meaning it generally contains elevated water saturation values within a specific range. This insight from actual geological conditions provides a critical constraint for constructing a more realistic model. Thus, we incorporate these boundary condition constraints, obtained from actual data analysis, into the loss function. The boundary conditions can be expressed as:

$$S_{min} < \widehat{S}_i < S_{max} \tag{21}$$

where S_{min} and S_{max} represent the minimum and maximum water saturation values in the study area (the specific values will be provided in Section 3.1). Based on these boundary conditions, the boundary loss function is formulated as:

$$\mathscr{L}_{Bc} = \frac{1}{2n} \sum_{i=1}^{n} (ReLU(\widehat{S}_i - S_{max}) + ReLU(\widehat{S}_i - S_{min})) \tag{22}$$

In this expression, *ReLU* is the rectified linear unit. Whenever $\widehat{S}_i$ exceeds the actual reservoir's upper or lower saturation limits, the model is penalized. By incorporating these features into the design of the loss function, the predicted results are more consistent with actual geological conditions, thereby enhancing the model's reliability and applicability. The overall loss function of the model is then defined as:

Table 1
Overview of wells and core sample data employed in this study.

Well	Depth (m)	Samples	Data type
TX8	5486–5570	108	Training dataset
TX11	5331–5438	71	Training dataset
TX12	5432–5526	89	Training dataset
TX15	5550–5629	58	Training dataset
TX23	5496–5582	68	Test dataset
TH9	5683–5697	14	Test dataset

$$\mathscr{L}_{Total} = \lambda_1 \mathscr{L}_{Data} + \lambda_2 \mathscr{L}_{Model} + \lambda_3 \mathscr{L}_{Bc} \tag{23}$$

where λ_1, λ_2 and λ_3 are hyperparameters that balance the three loss terms.

3. Data and training process

In this section, we describe the datasets used in this study, which include logging data and core experimental data for saturation prediction. We then detail the methodology utilized to convert original one-dimensional logging curves into two-dimensional geological feature maps suitable for SatuNN model input. Following that, we introduced a set of quantitative evaluation metrics to systematically compare the predictive efficacy of the proposed model. Finally, we outline the specific training procedures, detailing hyperparameter optimization processes, the implementation of physics-informed loss functions, and adaptive optimization methods employed during model training to enhance predictive performance, reliability, and generalization capabilities.

3.1. Datasets preparation

This study employs datasets consisting of logging data and corresponding core measurement data for reservoir saturation prediction. Specifically, a dataset containing petrophysical experimental results from ultra-deep tight sandstone gas reservoirs located in the Tuha Basin, northwest China, is utilized to train and test the proposed SatuNN model. Detailed information on the wells and samples is provided in Table 1. The dataset comprises a total of 408 labeled water saturation samples derived from core experiments conducted across eight wells. These measured data points serve as ground-truth labels for the supervised training and validation of the deep learning model. The input dataset includes ten logging curves: gamma ray (GR), spontaneous potential (SP), caliper (CAL), photoelectric absorption cross section (PE), deep resistivity (RD), shallow resistivity (RS), acoustic slowness (DT), compensated neutron logging (CNL), bulk density (DEN) and porosity (POR). The statistical distributions of these logging parameters are illustrated in Fig. 6(a–j). Additionally, Fig. 6(k) shows the water saturation distribution across the entire dataset, indicating that the reservoir water saturation in the study area primarily ranges from 20 % to 90 %, with an average value of 58 %. Notably, approximately 75 % of the samples have water saturations above 50 %, suggesting that these reservoirs typically exhibit a high water cut. In addition, the porosity of the reservoirs is extremely low (Fig. 6(j)), with a maximum porosity of less than 7 %, which reflects significant compaction and poses challenges for accurate saturation prediction. Data from wells TX23 and TH9 were selected as the test dataset, while the remaining wells were used for training, following a training-to-test ratio of approximately 0.8:0.2. This partitioning conforms to standard data division practices. Furthermore, the blind well data not used in training serve as an additional measure to

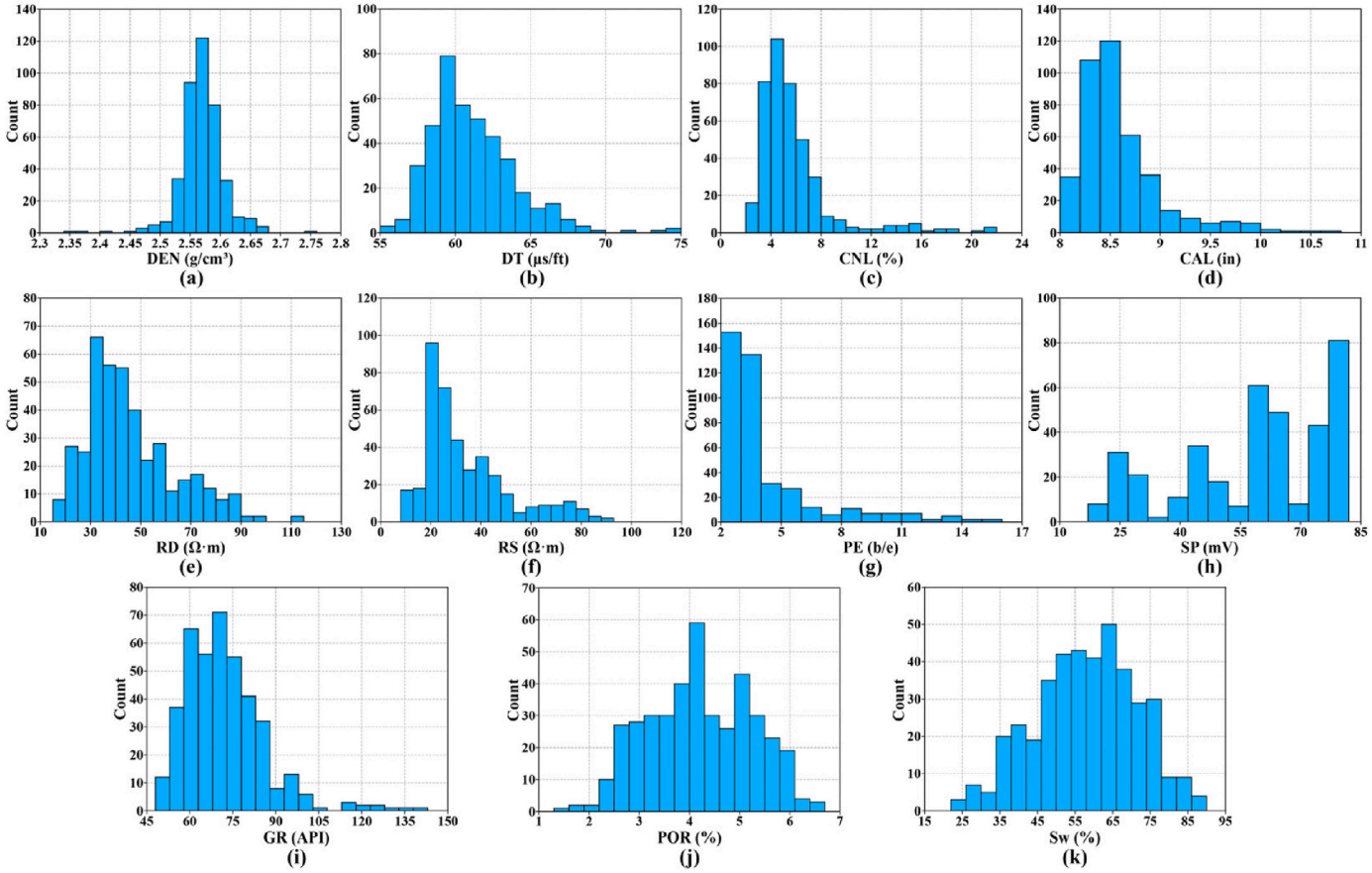

Fig. 6. Statistical distribution of logging parameters and reservoir water saturation. (a–j) Frequency histograms of ten conventional logging parameters including DEN, DT, CNL, CAL, RD, RS, PE, SP, GR, and POR. (k) Overall water saturation distribution illustrating a concentration range between 20 % and 90 %.

Depth	SP	GR	PE	CAL	DT	DEN	CNL	RD	RS	POR
5458	67.14	59.45	4.45	8.46	60.75	2.55	5.15	26.47	67.13	5.18

Normalization

Depth	SP	GR	PE	CAL	DT	DEN	CNL	RD	RS	POR
5458	0.7428	0.1146	0.1612	0.1087	0.1588	0.6269	0.1111	0.1063	0.0655	0.6792

2D image conversion

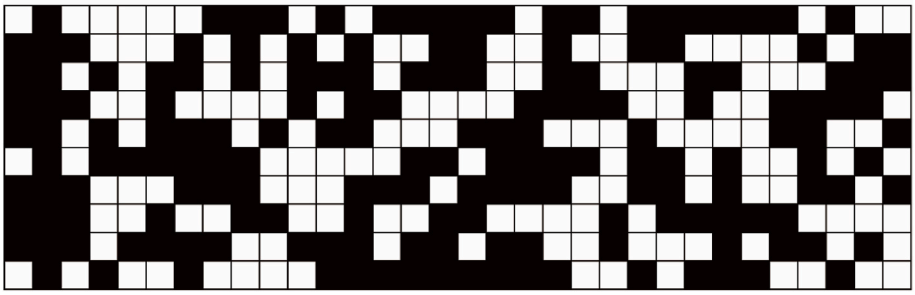

Fig. 7. Illustration of data normalization and two-dimensional image conversion. The original logging data at specific depth points (e.g., SP, GR, PE, CAL, DT, DEN, CNL, RD, RS and POR) are first normalized to ensure data scale consistency. These normalized values are then converted into binary (0 and 255) representations to form structured two-dimensional image matrices (geological feature maps).

evaluate the model's reliability, robustness, and generalization capability in predicting reservoir saturation for the study area.

As mentioned previously, the SatuNN model requires two-dimensional image data as input. Consequently, we convert the ten logging curves into two-dimensional geological feature maps, as illustrated in Fig. 7. These feature maps encode substantial geological and geophysical information pertinent to reservoir properties. Fig. 7 illustrates the process of converting ten logging curves at a specific depth point into a geological feature map. First, to eliminate inconsistencies in magnitude and range, the logging data are normalized using Eq. (24):

$$x_N = \frac{x - x_{min}}{x_{max} - x_{min}} \tag{24}$$

where x_{max} and x_{min} are the maximum and minimum values of the logging curve, respectively. Each of the ten normalized logging curves is then converted into a 32-bit binary string, producing a 10×32 matrix composed of zeros and ones. Next, the zeros and ones in this matrix are transformed into square images with pixel values of 0 and 255, respectively. These images are subsequently stacked to form a geological feature map, with each two-dimensional map corresponding to a single saturation data point at the matching depth (Fig. 7). For a more detailed description of this conversion process, please refer to Tian et al. (2024).

3.2. Performance evaluations

To rigorously evaluate the predictive accuracy of the proposed SatuNN model, we employ multiple quantitative performance metrics, including mean absolute error (MAE), mean absolute percentage error (MAPE), mean squared error (MSE) and the coefficient of determination (R^2). These metrics are mathematically defined as follows:

$$MAE = \frac{1}{N}\sum_{i=1}^{N}|y_i - \hat{y}_i| \tag{25}$$

$$MAPE = \frac{100\%}{N}\sum_{i=1}^{N}\frac{|y_i - \hat{y}_i|}{y_i} \tag{26}$$

$$MSE = \frac{1}{N}\sum_{i=1}^{N}(y_i - \hat{y}_i)^2 \tag{27}$$

$$R^2 = 1 - \frac{\sum_{i=1}^{N}(y_i - \hat{y}_i)^2}{\sum_{i=1}^{N}(y_i - aver(y_i))^2} \tag{28}$$

where y_i and $\hat{y}_i$ represent the true and predicted saturation values, respectively, $aver(y_i)$ denotes the mean of the true saturation values, and N is the number of samples. Given the strong heterogeneity of ultradeep tight reservoirs, we adopt multiple error metrics in conjunction with R^2 to evaluate model performance comprehensively. Different regression metrics exhibit varying sensitivities to bias and outliers, thereby offering a more robust assessment of predictive accuracy, particularly for datasets with large numerical ranges or uneven distributions. Meanwhile, the R^2 indicates how much variance in the target variable is captured by the model. Higher R^2 values, along with lower error metrics, imply superior predictive performance.

3.3. Model hyperparameters and training process

Following the SatuNN architecture shown in Fig. 1, our model uses two feature extraction pathways. The first pathway converts normalized logging data into two-dimensional geological feature maps, which are then processed by two CW Blocks. Each CW Block comprises two-dimensional convolutional layers and window attention mechanisms to extract spatial features. These outputs subsequently pass through three BA Blocks, each containing a BiLSTM network, an axial attention mechanism, and a layer normalization layer. The second pathway takes the raw logging curves as input, using three BA Blocks to extract latent temporal features. The high-dimensional representations from both pathways are concatenated and then fed into fully connected layers for saturation prediction. All experiments were implemented in PyTorch and trained on an NVIDIA RTX 4060Ti GPU with 16 GB of memory. Referring to the training flowchart in Fig. 5, we adopt a physics-informed neural network (PINN)-based loss function that incorporates geological prior information to reduce discrepancies between the

Table 2
Hyperparameter settings for the proposed SatuNN model.

Network hyperparameter	Value
Kernel size (2-D convolutional layer) k	2
Filters (2-D convolutional layer) f	64
BiLSTM units c	32
Window size	2
Attention heads	8
Batch size	16
Initial learning rate	0.005

predicted and true saturation values. We set the weights of the data loss λ_1 and model loss λ_2 to 1. Additionally, the weight of the boundary conditions λ_3 is set smaller as an auxiliary loss, ensuring it assists in correcting model predictions without excessively influencing the primary optimization objectives. After multiple ablation experiments, the hyperparameter λ_3 was finally determined as 0.6. This loss function minimizes the difference between true and predicted saturation values, and also incorporates critical petrophysical features and constraints from geological priors, thus allowing the training process to balance data-driven accuracy and physical consistency. Based on the analysis in Section 3.1, the boundary conditions for water saturation in the loss function are set to 20 % and 90 %. By integrating critical petrophysical constraints into the training process, the model achieves a balance between data-driven accuracy and physical consistency, generating predictions that align well with both geological principles and core data.

We reserve 15 % of the training data as a validation set, utilized for performance evaluation after each epoch or several mini-batches. Simultaneously, the Adam optimization algorithm is employed to minimize the loss function, with an initial learning rate of 0.005. To prevent gradient vanishing during network iterations, we implement early stopping and adaptive learning rate optimization algorithms. Specifically, if the prediction error on the validation set did not decrease for 50 consecutive epochs, the learning rate was reduced by a factor of 2 Training terminated when the validation set prediction error failed to decrease further over 100 consecutive epochs, preserving the best-performing model based on the lowest validation prediction error. Additionally, we utilized Optuna—a Python-based open-source hyperparameter optimization library—for hyperparameter tuning. Optuna employs efficient search algorithms (e.g., TPE, CMA-ES) within a given search space to automatically identify optimal hyperparameter combinations. After hyperparameter tuning through validation experiments, we finalize the hyperparameters of SatuNN as shown in Table 2. In particular, within the CW Block, the kernel size (k) of the 2-D convolutional layers was set to 2, the number of filters (f) was set to 64, and the window size for window attention was set to 2. Within the BA Block, the number of BiLSTM units (c) was set to 32. The batch size is determined to be 16 through the hyperparameter search process.

4. Result and analysis

4.1. Assessing model performance: a comparative analysis

In this experiment, data from wells TX23 and TH9 served as the test dataset, whereas data from the remaining four wells were employed as the training set. Dataset characteristics and the training approach were previously detailed in Section 3. To examine the influence of the two attention mechanisms in SatuNN, the proposed network was decomposed into three baseline variants: one without window attention (Without WA) in the CW Block, one without axial attention (Without AA) in the BA Block, and a fully BiLSTM network omitting both WA and AA. All baseline models were trained using the PINN framework. Additionally, to specifically assess the impact of embedding petrophysical constraints, we introduce a purely data-driven variant (Without PINN) that retains the complete SatuNN architecture but excludes the physics-informed neural network component entirely. Furthermore, predictions from the conventional Archie petrophysical model were utilized as an additional benchmark. Fig. 8 illustrates the correlation coefficient matrix between the input logging parameters and the saturation labels in the test dataset. Intuitively, stronger correlations between input parameters and the target variable facilitate more straightforward prediction. As shown in Fig. 8, porosity exhibits the most significant negative correlation with saturation, whereas other logging curves display relatively weak correlations. This observation

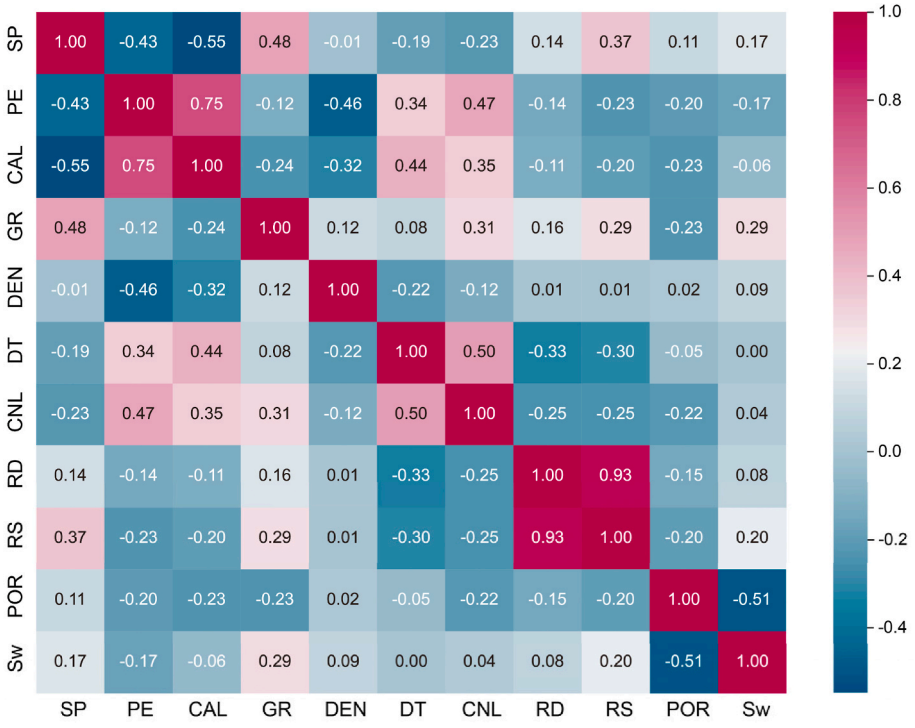

Fig. 8. Correlation coefficient matrix between logging parameters and reservoir water saturation in the test dataset.

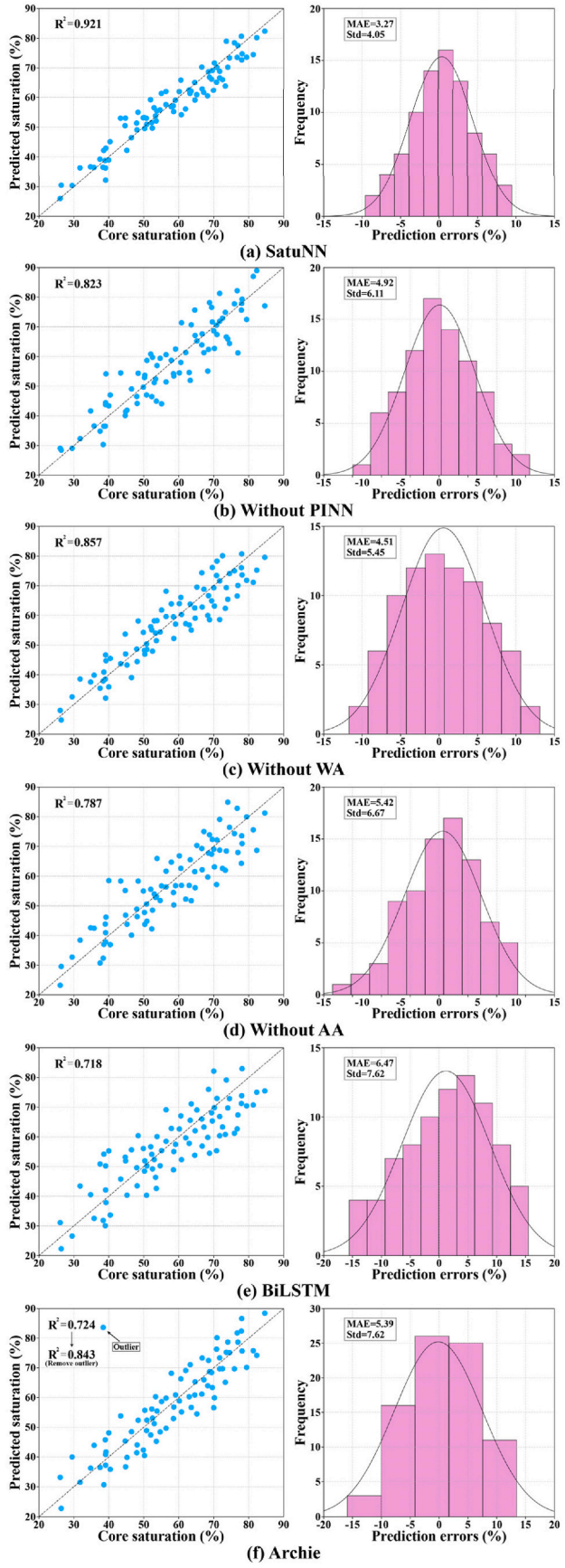

Fig. 9. Comparison of predicted versus measured water saturation values and corresponding error analyses for different models in the test dataset.

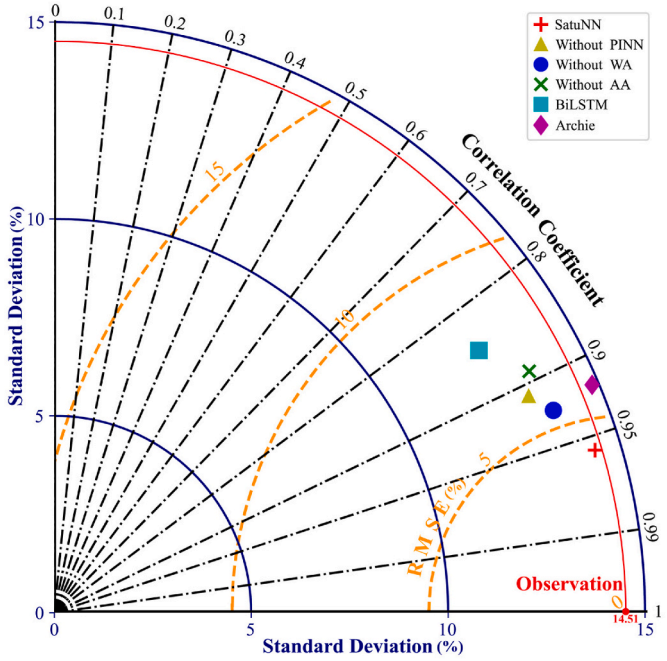

Fig. 10. Taylor diagram comparing model performance metrics.

suggests that a simplistic linear correlation between logging parameters and saturation is inadequate for precise reservoir characterization, underscoring the necessity of sophisticated nonlinear modeling strategies.

Fig. 9 compares the saturation predictions of different models against the actual core saturation data in the test dataset, accompanied by corresponding error histograms. The scatter plots (left panel) illustrate the agreement between predicted and measured values, while the error histograms (right panel) reflect the distribution of prediction residuals. Among all the methods evaluated, the proposed SatuNN model achieves the highest coefficient of determination (R^2 = 0.921), indicating a robust correlation between predictions and true measurements. Data points for SatuNN cluster tightly around the ideal 1:1 line, affirming the model's capability to capture complex nonlinear reservoir properties effectively. Furthermore, the prediction error histogram for SatuNN reveals a narrow, zero-centered distribution with the lowest mean absolute error (MAE = 3.27 %) and standard deviation (Std = 4.05 %), underscoring its robustness and precision (Fig. 9(a)). By contrast, the Without PINN, Without WA and Without AA model demonstrate reduced performance, with R^2 values of 0.823, 0.857 and 0.787, respectively (Fig. 9(b–d)). Their scatter plots show larger deviations from the 1:1 line, broader error distributions, and higher MAEs (4.92 %, 4.51 % and 5.42 %). Similarly, the BiLSTM model (fully omitting window and axial attention) attains the lowest R^2 (0.718) and the highest MAE (6.47 %), indicating its limited predictive capacity (Fig. 9(e)). Meanwhile, the Archie model achieves an R^2 of 0.843 (after outlier removal), but its MAE (4.83 %) and error distribution remain inferior to those of SatuNN (Fig. 9(f)). Collectively, these results affirm that SatuNN consistently outperforms all comparative methods in accuracy and error minimization, validating its suitability and superiority for saturation prediction in complex reservoir.

Although scatter plots provide valuable insights into prediction accuracy, they have limitations in comprehensively evaluating model performance using multiple metrics (Zhu et al., 2024). The Taylor diagram (Fig. 10) addresses this limitation by combining correlation coefficient, standard deviation, and root mean square error into one intuitive chart. In Fig. 10, the red circle represents the observed (true) saturation values, and the radial distance, angle, and arc correspond to the standard deviation, correlation coefficient, and RMSE, respectively. The

Table 3
Summary of standard deviation (Std), root-mean-square error (RMSE), and correlation coefficient (r) for various models.

Models	Std (%)	RMSE (%)	r (−)
SatuNN	14.33	4.05	0.96
Without PINN	13.31	6.11	0.91
Without WA	13.69	5.45	0.93
Without AA	13.52	6.67	0.89
BiLSTM	12.67	7.62	0.85
Archie (remove outlier)	14.78	5.74	0.92

Table 4
Quantitative comparison of four statistical metrics across evaluated models on the test dataset.

Models	MAE (%)	MAPE (%)	MSE (%)	R^2 (−)
SatuNN	3.27	5.91	16.40	0.92
Without PINN	4.92	8.84	37.37	0.82
Without WA	4.51	7.97	29.70	0.86
Without AA	5.42	9.93	44.49	0.79
BiLSTM	6.47	11.97	58.06	0.72
Archie	4.83	8.96	32.95	0.84

SatuNN marker (red cross) is positioned near a correlation coefficient of 0.95, significantly higher than those of the other methods, and its standard deviation is closest to that of the observed data (red arc). By comparison, the Without PINN (yellow triangle), Without WA (blue circle) and Without AA (green cross) models achieve correlation coefficients of 0.91, 0.93 and 0.89, respectively, but deviate more from the observed standard deviation. The BiLSTM network (cyan square) has the lowest correlation coefficient (r = 0.85) and the highest root mean square error (RMSE = 7.62), underscoring its inability to capture key data features. Although the Archie model (purple diamond, with outliers removed) shows a standard deviation somewhat closer to the observations than the Without WA model, its RMSE remains relatively large. Specific parameters of the models illustrated in Fig. 10 are provided in Table 3.

To quantitatively assess and compare predictive performance, four statistical metrics for all models were calculated, as summarized in Table 4. Clearly, SatuNN demonstrates superior predictive accuracy, achieving the lowest errors across all metrics and the highest R^2 value in blind well tests. Fig. 11 further emphasizes these results through direct comparative visualizations. Specifically, SatuNN attains an MAE of 3.27 %, significantly lower than those for Without PINN (4.92 %), Without WA (4.51 %), Without AA (5.42 %), BiLSTM (6.47 %), and Archie (4.83 %) (Fig. 11(a)). Similarly, the mean absolute percentage error (MAPE) for SatuNN is markedly lower at 5.91 %, compared with 8.84 %, 7.97 %, 9.93 %, 11.97 %, and 8.96 % for Without WA, Without AA, BiLSTM, and Archie, respectively (Fig. 11(b)). Remarkably, the R^2 achieved by SatuNN (0.92) notably exceeds those of the conventional Archie method (0.84) and the ablated variants (Without PINN: 0.82; Without WA: 0.86; Without AA: 0.79). Although Without WA performs best among the baseline models, SatuNN outperforms it by 27.49 %, 25.85 %, 44.78 %, and 6.98 % in MAE, MAPE, MSE, and R^2, respectively. These outcomes conclusively demonstrate that SatuNN offers enhanced accuracy, reliability, and robustness for predicting water saturation in ultradeep tight sandstone reservoirs.

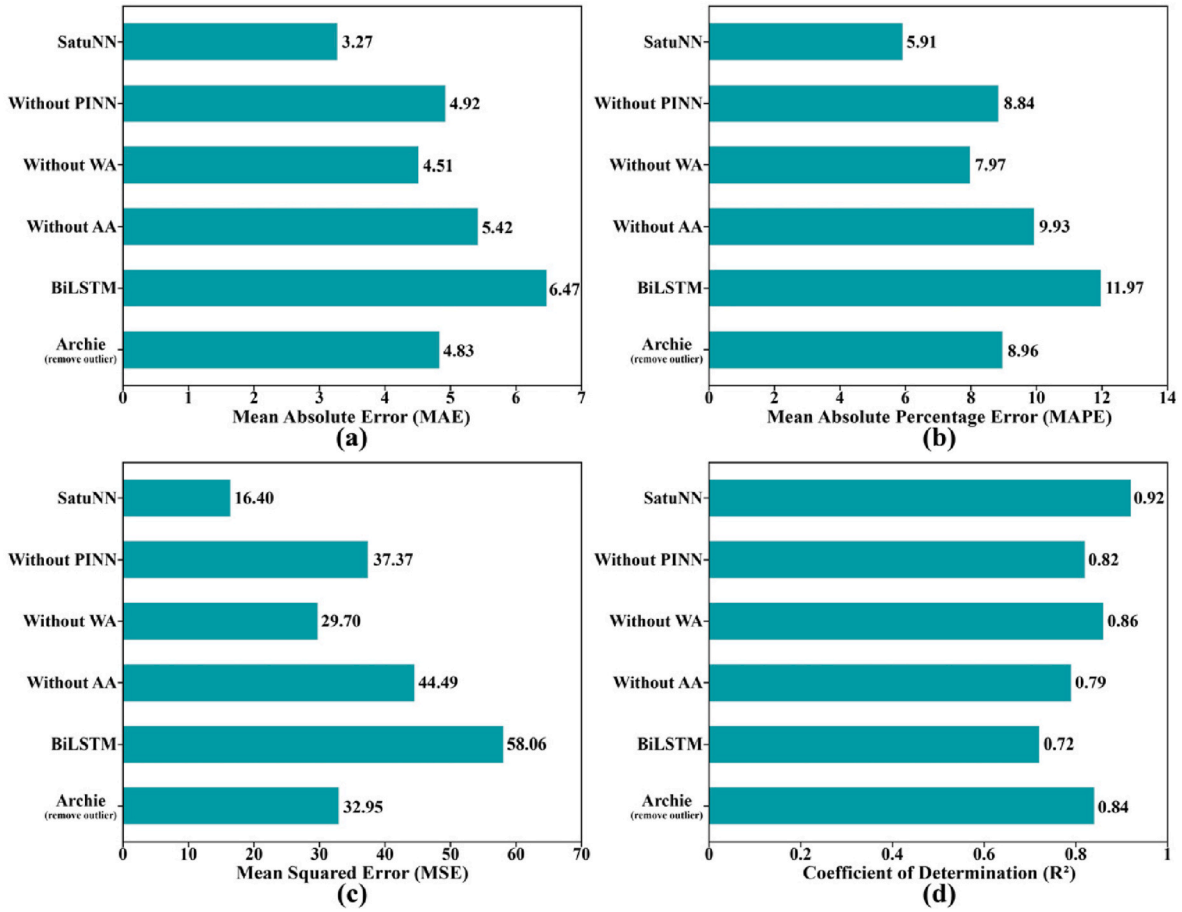

Fig. 11. Comparison of prediction metrics among evaluated models.

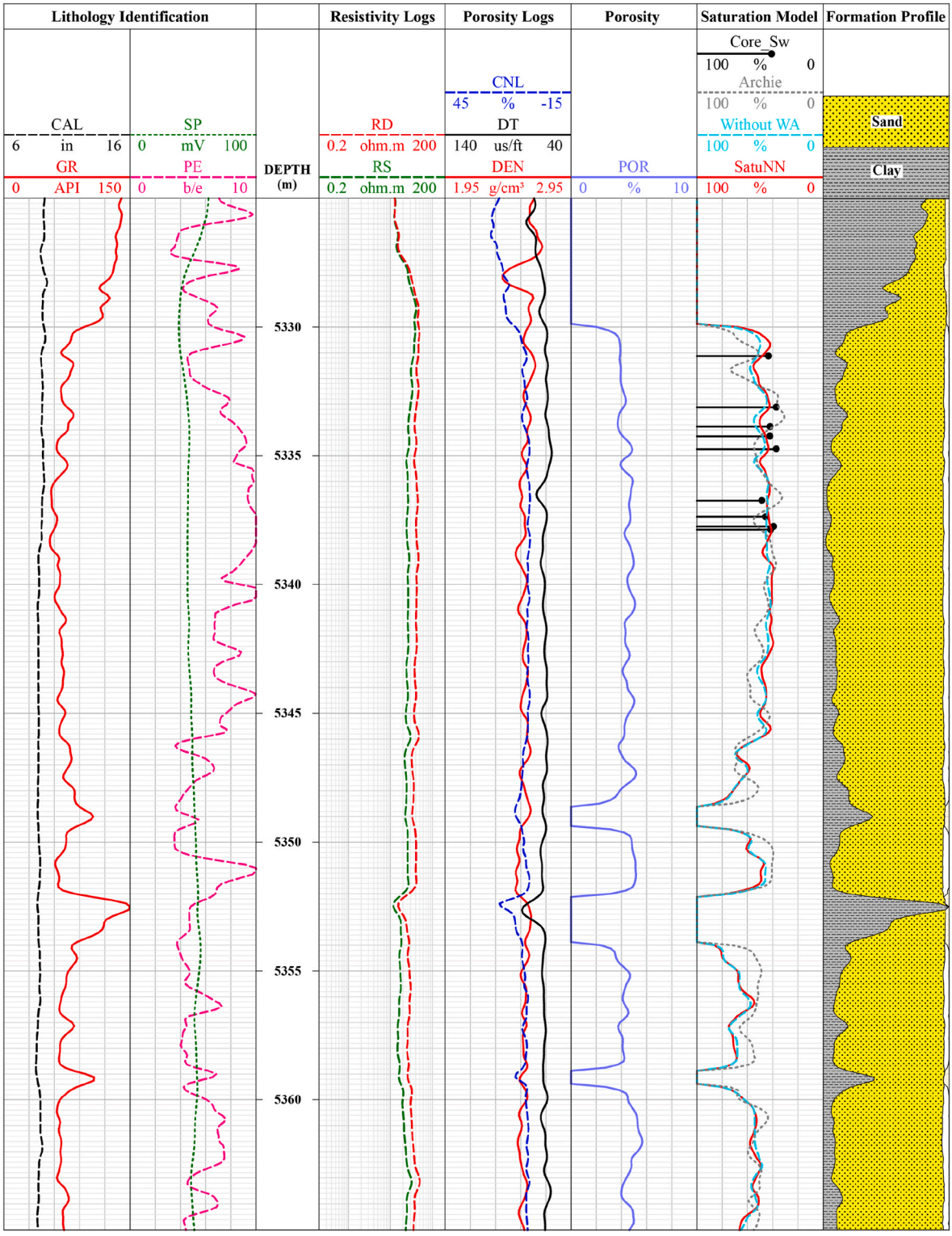

Fig. 12. Comparative well log interpretation and saturation predictions for the Jurassic Sangonghe Formation in Well Ji7, Tuha Basin. Tracks 1–6 illustrate logging curves including SP, GR, CAL, PE, RD, RS, DT, CNL, DEN and POR. Track 7 compares core measured water saturation values with predictions from the proposed SatuNN model, the Without Window Attention (Without WA) variant, and the traditional Archie method. SatuNN exhibit the closest agreement with core data.

4.2. A comparative analysis of saturation prediction models in core well profile: case studies

This section applies the previously established saturation prediction model to actual tight sandstone reservoirs in the Tuha Basin, focusing on two wells designated Ji7 and Ji7-2-3H. Each well exhibits ultra-low porosity and permeability, posing challenges for conventional saturation estimation methods. By comparing the proposed Saturation Neural Network (SatuNN) with other approaches, we demonstrate the practical benefits and reliability of the new model under complex reservoir conditions.

Well Ji7 is a pilot well located in the Taipei Depression of the Tuha

Table 5
Quantitative comparison of saturation prediction errors for well Ji7.

Models	MAE (%)	MAPE (%)	MSE (%)
SatuNN	4.13	10.06	21.48
Without WA	6.75	16.63	60.33
Archie	9.23	22.12	109.91

Basin, China. The target interval lies within the Jurassic Sangonghe Formation, predominantly consisting of tight sandstone. Ten logging curves were utilized as inputs: nine conventional logging measurements—spontaneous potential (SP), gamma ray (GR), caliper (CAL), photoelectric absorption cross section (PE), deep resistivity (RD), shallow resistivity (RS), acoustic slowness (DT), compensated neutron logging (CNL), and bulk density (DEN)—plus a derived porosity (POR) curve. Traditionally, empirical models such as Archie's formula have been employed to interpret water saturation in this interval. However, due to the extremely tight nature of the formation, these methods have shown limited accuracy in practical applications. Fig. 12 displays the prediction results from three different models (including SatuNN) across the Ji7 reservoir interval. The first six tracks show the original logging curves, and the seventh track compares the predicted water saturations against laboratory core measurements. Among the tested methods, SatuNN aligns most closely with the core data, indicating that it effectively captures the complex nonlinear relationships underlying water saturation in tight sandstone reservoirs. Table 5 further illustrates these findings by listing three error metrics for each model. SatuNN achieves a MAE of 4.13 %, a MAPE of 10.06 %, and a MSE of 21.48 %. In comparison, the variant without window attention (Without WA) and the traditional Archie model exhibits significantly higher error values, reinforcing the superior performance and robustness of SatuNN for saturation prediction in the Ji7 well.

To further validate the model's generalization capability, we applied the same prediction methodology to a second well, Ji7-2-3H, located in the same basin but featuring different reservoir characteristics. Figs. 13 and 14, along with Table 6, summarize the results and provide a detailed performance comparison among SatuNN, the Without WA variant, and the Archie method. Fig. 13 compares the predicted water saturation profiles with core laboratory measurements along the reservoir interval of Ji7-2-3H. As with Well Ji7, SatuNN's predictions show excellent agreement with the core-derived values, indicating that the model successfully adapts to the geological variations in this second well. In contrast, the Without WA model and the Archie method exhibit larger deviations from the core data, highlighting their reduced reliability in characterizing ultradeep tight reservoirs. Table 6 quantifies the predictive performance of the three methods. SatuNN maintains the lowest MAE (4.53 %), MAPE (8.09 %), and MSE (31.35 %). By comparison, the Without WA model records higher errors (MAE = 6.52 %; MSE = 70.44 %), and the Archie approach demonstrates the largest discrepancies (MAE = 14.11 %; MSE = 310.72 %). These metrics clearly underscore the benefits of integrating window attention, axial attention, and a physics-informed loss function, as implemented in the SatuNN framework. Fig. 14 provides a detailed evaluation of the performance of the SatuNN model in well Ji7-2-3H. The left panel illustrates a comparison between the predicted water saturation values obtained by the proposed SatuNN model and the core-measured saturation values. The predicted results closely align with the ideal 1:1 reference line, indicating strong agreement with actual measurements. The proposed SatuNN achieves a coefficient of determination (R^2) of approximately 0.92, confirming excellent predictive accuracy in this ultradeep tight sandstone reservoir. Furthermore, the prediction residual distribution on the right panel of the figure exhibits a narrow and symmetric pattern centered around zero, underscoring minimal systematic bias and strong prediction stability. The computed MAE and MAPE for SatuNN are significantly lower than those for the benchmark models (as detailed in Table 6), clearly illustrating the effectiveness and robustness of our model. This scatter plot and residual distribution analysis collectively demonstrate the high precision, stability, and generalization capability of SatuNN, effectively validating its practical applicability in saturation prediction tasks under complex reservoir conditions.

Overall, the comparative analyses in Wells Ji7 and Ji7-2-3H confirm that SatuNN achieves superior prediction accuracy, lower error metrics, and closer alignment with core measurements compared to both ablation models and the empirical Archie method. By integrating two-dimensional geological feature mapping, windowed and axial attention mechanisms, and a physics-informed neural network loss function, SatuNN captures the multifaceted conduction pathways and petrophysical heterogeneities characteristic of ultradeep tight reservoirs. Importantly, the data from these two wells were completely independent of both training and test datasets, demonstrating the robustness of SatuNN to variations in input data. From an operational perspective, these results suggest that SatuNN can serve as a reliable tool for reservoir characterization and fluid distribution analysis in complex tight sandstone settings. Enhanced saturation estimation not only reduces the need for extensive core sampling but also aids in more accurate resource evaluation, better completion strategies, and improved reservoir management.

4.3. Roles of attention mechanisms and advantages of the PINN framework

The proposed model integrates two distinct attention mechanisms—window attention (WA) and axial attention (AA)—to capture both local and global features in logging data. WA operates on localized "windows" of the input feature maps, thereby emphasizing critical local spatial variations. In ultradeep tight sandstone reservoirs, subtle heterogeneities (e.g., microfractures, localized clay distributions) can significantly influence fluid flow and conductivity (Cai et al., 2017). By adaptively adjusting feature weights within these localized regions, WA helps the network learn fine-grained geological information, improving the accuracy of saturation predictions. AA processes data along different axial dimensions (e.g., depth, lateral extents) to capture long-range dependencies and overall structural continuity. Unlike WA, which focuses on local receptive fields, AA ensures that the model considers the broader geological context. This is especially valuable for identifying large-scale reservoir trends and correlating zones of similar petrophysical characteristics across different intervals. The results of the ablation studies (Tables 3–6, Figs. 9–14) clearly illustrate the effectiveness of both attention mechanisms. For instance, the removal of WA or AA components individually leads to notable declines in predictive accuracy, with higher prediction errors and decreased correlation metrics observed. Fig. 15 demonstrates the impacts of the window attention (WA) and axial attention (AA) mechanisms within the proposed SatuNN model by comparing the residuals of predicted saturation from the test dataset with the core data. The horizontal axis indicates the predicted water saturation values, whereas the vertical axis displays corresponding prediction errors (core measurements minus model predictions). The residual distribution for the SatuNN model (blue markers) closely concentrates around the zero-error line, reflecting minimal error and higher prediction accuracy. By contrast, removing window attention or axial attention results in greater dispersion of errors, particularly at moderate-to-high predicted saturations. These observations underscore the complementary roles of both attention mechanisms in capturing reservoir heterogeneity. The combined effect of these two mechanisms enhances the model's ability to detect both small-scale and large-scale variations, ultimately improving the accuracy and robustness of the saturation predictions.

To assess the impact of the physical constraints, a purely data-driven variant (Without PINN) was constructed using the identical SatuNN architecture but excluding the physics-informed neural network component. The Without PINN achieved respectable predictive accuracy on the test dataset ($R^2 = 0.82$, MAE = 4.92 %), ranking third among all

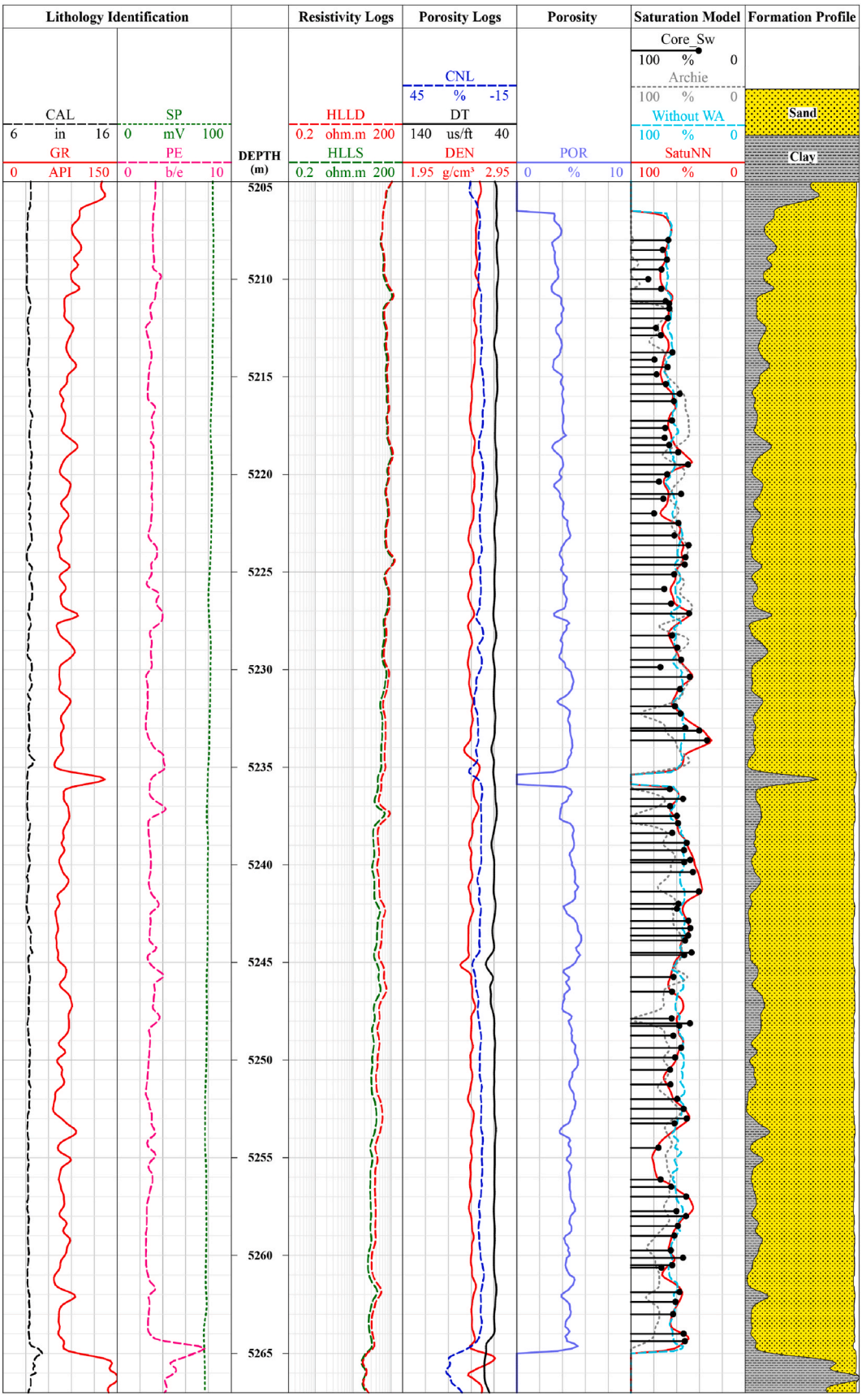

Fig. 13. Comparative well log interpretation and saturation predictions for the Jurassic Sangonghe Formation in Well Ji7-2-3H, Tuha Basin. Saturation predictions by SatuNN align closely with core derived measurements, demonstrating improved accuracy and robustness compared to the Without WA and Archie methods.

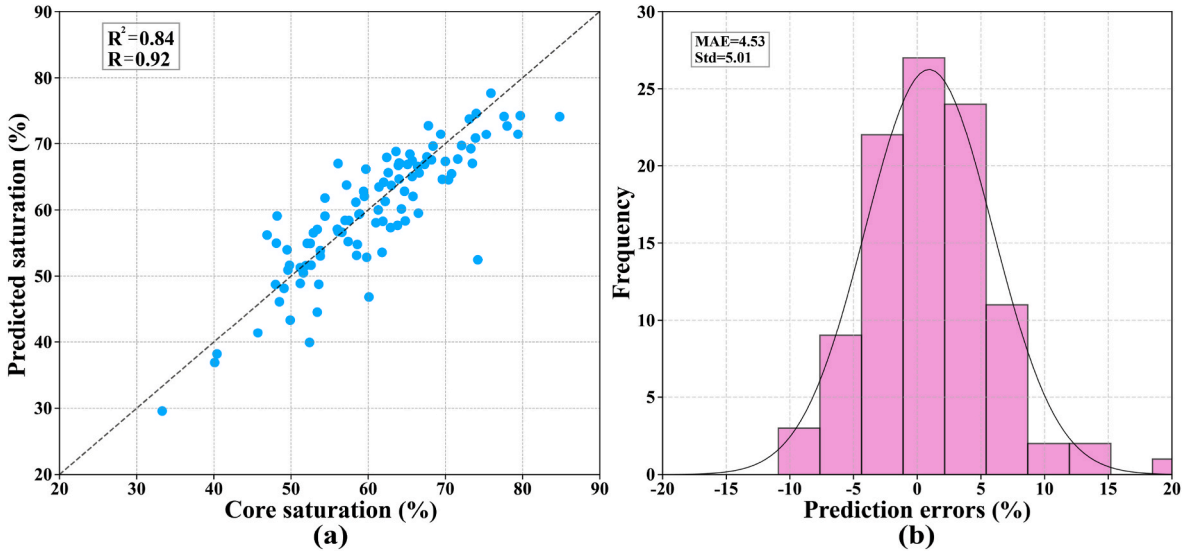

Fig. 14. Detailed predictive performance of SatuNN in Well Ji7-2-3H. (a) Scatter plot contrasting SatuNN-predicted water saturation values against core measurements. (b) Histogram of prediction errors.

Table 6
Quantitative comparison of saturation prediction errors for well Ji7-2-3H.

Models	MAE (%)	MAPE (%)	MSE (%)
SatuNN	4.53	8.09	31.35
Without WA	6.52	11.93	70.44
Archie	14.11	24.38	310.72

deep learning baselines—behind only the SatuNN (R^2 = 0.92, MAE = 3.27 %) and Without WA (R^2 = 0.86, MAE = 4.51 %), yet outperforming the Without AA and BiLSTM (Table 6, Figs. 9 and 11). This outcome demonstrates that the fundamental SatuNN architecture itself provides notable performance advantages through its sophisticated integration of specialized modules (e.g., CNN, BiLSTM, window and axial attention mechanisms). However, the marked improvement in accuracy observed upon introduction of PINN (SatuNN) confirms the substantial added value of embedding geological constraints. In particular, incorporating PINN produces a transformative increase in predictive accuracy, demonstrating that constraints grounded in reservoir petrophysics align the SatuNN' outputs more closely with core saturation data and steer its performance toward an optimal, regionally applicable solution. Furthermore, differences in input dimensionality across the ablation models highlight the importance of matching input data structures with suitable model architectures. For example, the BiLSTM model processes only one-dimensional logging data and inherently cannot incorporate two-dimensional geological feature maps. This model architectural limitation prevents integration of higher-dimensional inputs and limits the stratigraphic information that can be captured. Consequently, restricted input dimensionality and the model's inherent structure largely explains its weaker performance. Overall, this comprehensive comparison clearly demonstrates that incorporating petrophysics constraints derived from geological feature via the PINN framework

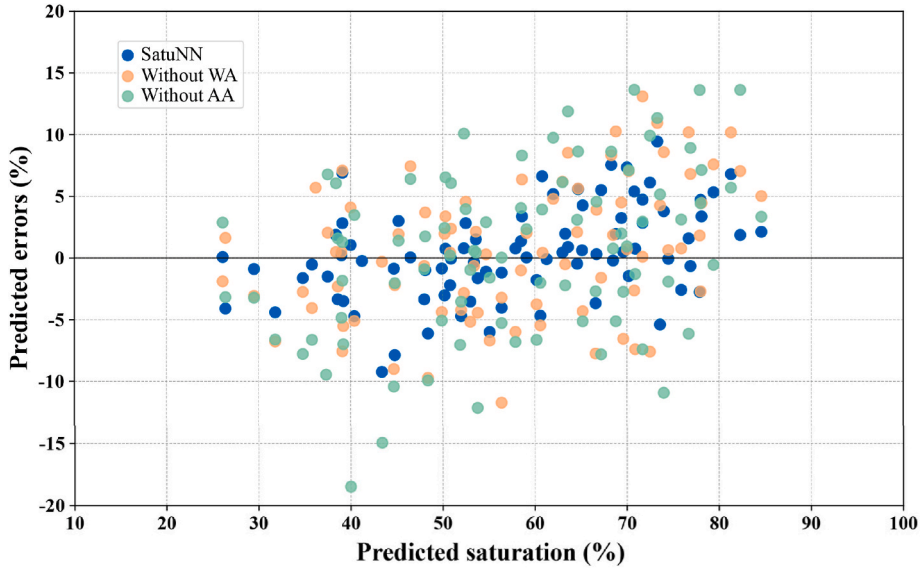

Fig. 15. Residual analysis of SatuNN vs. ablated models (Without WA/AA) on the test dataset. Blue markers show the full SatuNN model, exhibiting minimal deviations around the zero-error line, indicating higher accuracy. The variants omitting window attention (Without WA, orange markers) or axial attention (Without AA, green markers) demonstrate increased dispersion and greater error magnitudes. (For interpretation of the references to colour in this figure legend, the reader is referred to the Web version of this article.)

significantly enhances model accuracy and robustness. By embedding petrophysical constraints directly into the network via the Physics-Informed Neural Network (PINN) framework, the model ensures consistency with fundamental reservoir properties and conduction mechanisms. Incorporating established petrophysical equations (e.g., Hanai–Bruggeman or effective medium theories) into the loss function constrains the model to generate geologically feasible predictions. Physics-based terms in the loss function act as regularizers, guiding the model toward physically meaningful solutions (Lu et al., 2024). This is particularly beneficial when training datasets are limited or exhibit heterogeneous distributions. Although deep learning methods often appear as "black boxes" enforcing physical constraints helps interpret predictions in light of reservoir properties, fostering greater trust among geoscientists and engineers.

4.4. Existing issues and future work prospects

Accurate and robust prediction of reservoir parameters is essential for optimizing exploration and production strategies in oil and gas fields. In this study, we developed and validated a deep learning framework (SatuNN) utilizing conventional logging data for reservoir water saturation prediction. Nevertheless, despite the promising results demonstrated, our approach remains subject to several limitations that merit further consideration. Specifically, the effectiveness of our model relies significantly on the availability, quality, and representativeness of input logging datasets. Given the intrinsic limitations associated with conventional logging data—such as restricted spatial coverage, measurement uncertainty, and limited sensitivity to subtle reservoir features—model performance may decline in situations characterized by inadequate or low-quality data.

To address these limitations and further improve predictive accuracy and generalizability, future research should prioritize the integration of diversified geoscience datasets, such as advanced logging techniques, seismic attributes, and geochemical analyses. Advanced logging methods (e.g., imaging logs and nuclear magnetic resonance logs) provide high-resolution insights into pore geometry, fluid distributions, and detailed lithological characteristics, thereby offering richer information for modeling complex reservoir heterogeneities (Kuang et al., 2021). Additionally, integrating seismic and geochemical data could offer critical insights into larger-scale reservoir continuity, hydrocarbon distribution, and reservoir quality variations, thus enhancing the model's predictive capabilities across multiple scales (Roques et al., 2020). Moreover, considering that the current study predominantly focuses on tight sandstone reservoirs characterized by clastic porous media, it is crucial to evaluate and expand the applicability of the SatuNN and PINN methodologies to other reservoir types, including carbonate reservoirs, shale formations, and mixed lithology systems. Each of these reservoir types exhibits distinct pore architectures, conduction mechanisms, and fluid interactions that differ significantly from tight sandstones. Thus, future work should aim to develop customized petrophysical models and physics-informed constraints specifically tailored to distinct reservoir types. Such targeted adjustments can ensure that the proposed deep learning framework maintains superior predictive performance, interpretability, and reliability across diverse geological contexts.

5. Conclusion

In this paper, we proposed a novel deep learning framework, SatuNN, to accurately predict water saturation in ultradeep tight sandstone reservoirs. By combining two-dimensional convolutional neural networks with window attention, bidirectional long short-term memory layers with axial attention, and physics-informed neural network constraints, our method captures multiscale spatial and temporal features while ensuring consistency with fundamental petrophysical principles. Extensive experiments on actual reservoir data from the Tuha Basin demonstrated that SatuNN achieves higher accuracy and lower prediction errors compared to conventional empirical methods and ablated deep learning variants. A key advantage of the proposed approach lies in its ability to integrate advanced attention mechanisms with physics-based constraints, which improves interpretability and guards against overfitting. Moreover, the model's two-pathway structure, utilizing both transformed two-dimensional geological feature maps and raw logging curves, effectively mitigates information loss and enhances predictive robustness. Nevertheless, the success of the model depends on data availability and quality, and additional work is needed to validate its adaptability to other reservoir types such as carbonates, shales, and fractured formations. Overall, SatuNN represents a promising solution for reservoir evaluation in complex geologic settings, offering more reliable and physically consistent predictions of water saturation.

CRediT authorship contribution statement

Yinhong Tian: Writing – review & editing, Writing – original draft, Software, Methodology, Investigation, Formal analysis, Data curation, Conceptualization. **Guiwen Wang:** Supervision, Software, Resources, Project administration, Funding acquisition, Conceptualization. **Hongbin Li:** Writing – review & editing, Validation, Software. **Jin Lai:** Writing – review & editing, Resources, Project administration.

Declaration of competing interest

The authors declare that they have no known competing financial interests or personal relationships that could have appeared to influence the work reported in this paper.

Acknowledgment

This work was jointly supported by "National Natural Science Foundation of China" (Grant No. 41872133, 42002133); "CNPC Key S&T Special Project" (Grant No. 2022DJ2107).

Data availability

The authors do not have permission to share data.

References

Afrapoli, M.S., Crescente, C., Alipour, S., Torsaeter, O., 2009. The effect of bacterial solution on the wettability index and residual oil saturation in sandstone. J. Petrol. Sci. Eng. 69 (3–4), 255–260.

Afrasiabi, S., Afrasiabi, M., Jarrahi, M.A., Mohammadi, M., Aghaei, J., Javadi, M.S., Shafie-Khah, M., Catalao, J.P.S., 2021. Wide-area composite load parameter identification based on multi-residual deep neural network. IEEE Trans. Neural. Netw. Learn. Syst. 34 (9), 6121–6131.

Al-Bulushi, N., King, P.R., Blunt, M.J., Kraaijveld, M., 2009. Development of artificial neural network models for predicting water saturation and fluid distribution. J. Petrol. Sci. Eng. 68 (3–4), 197–208.

Almajid, M.M., Abu-Al-Saud, M.O., 2022. Prediction of porous media fluid flow using physics informed neural networks. J. Petrol. Sci. Eng. 208.

Ameur-Zaimeche, O., Kechiched, R., Heddam, S., Wood, D.A., 2022. Real-time porosity prediction using gas-while-drilling data and machine learning with reservoir associated gas: case study for hassi Messaoud field. Algeria. Mar. Petrol. Geol. 140.

Amiri, M., Ghiasi-Freez, J., Golkar, B., Hatampour, A., 2015. Improving water saturation estimation in a tight shaly sandstone reservoir using artificial neural network optimized by imperialist competitive algorithm – a case study. J. Petrol. Sci. Eng. 127, 347–358.

Amiri, M., Yunan, M.H., Zahedi, G., Jaafar, M.Z., Oyinloye, E.O., 2012. Introducing new method to improve log derived saturation estimation in tight shaly sandstones—A case study from Mesaverde tight gas reservoir. J. Petrol. Sci. Eng. 92–93, 132–142.

Archie, G.E., 1942. The electrical resistivity log as an aid in determining some reservoir characteristics. OR Trans. 146 (1), 54–62.

Bai, Y., Tan, M., Cao, H., Tang, J., Liang, Z., 2022a. Intelligent classification of carbonate reservoir quality using multisource geophysical logging and seismic data. IEEE Trans. Geosci. Remote. Sens. 60, 1–12.

Bai, Y., Tan, M., Shi, Y., Zhang, H., Li, G., 2022b. Regression Committee machine and petrophysical model jointly driven parameters prediction from wireline logs in tight sandstone reservoirs. IEEE Trans. Geosci. Remote. Sens. 60, 1–9.

Baziar, S., Shahripour, H.B., Tadayoni, M., Nabi-Bidhendi, M., 2016. Prediction of water saturation in a tight gas sandstone reservoir by using four intelligent methods: a comparative study. Neural Comput. Appl. 30 (4), 1171–1185.
Bergen, K.J., Johnson, P.A., de Hoop, M.V., Beroza, G.C., 2019. Machine learning for data-driven discovery in solid Earth geoscience. Science 363 (6433), eaau0323.
Bruggman, D.A.G., 1935. Berechnung verschiedener physikalisher Konstanten von heterogenen Substanzen. Ann. Phys. 416 (7), 636–664.
Bussian, A., 1983. Electrical conductance in a porous medium. Geophysics 48 (9), 1258–1268.
Cai, J., Wei, W., Hu, X., Wood, D.A., 2017. Electrical conductivity models in saturated porous media: a review. Earth Sci. Rev. 171, 419–433.
Chakraborty, A., Rabinovich, A., Moreno, Z., 2025. A data-driven physics-informed deep learning approach for estimating sub-core permeability from coreflooding saturation measurements. Adv. Water Resour. 198.
Chen, T., et al., 2024. Prestack seismic inversion driven by priori information neural network and statistical characteristic. IEEE Trans. Geosci. Remote. Sens. 62, 1–14.
Chen, W., Yang, L., Zha, B., Zhang, M., Chen, Y., 2020. Deep learning reservoir porosity prediction based on multilayer long short-term memory network. Geophysics 85 (4), WA213–WA225.
Clavier, C., Coates, G., Dumanoir, J., 1984. Theoretical and experimental bases for the dual-water model for interpretation of Shaly sands. SPE J. 24 (2), 153–168.
de Lima, R.P., Duarte, D., Nicholson, C., Slatt, R., Marfurt, K.J., 2020. Petrographic microfacies classification with deep convolutional neural networks. Comput. Geosci-Uk. 142, 104481.
Dong, X., et al., 2022. Seismic shot gather denoising by using a supervised-deep-learning method with weak dependence on real noise data: a solution to the lack of real noise data. Surv. Geophys. 43 (5), 1363–1394.
dos Santos, D.T., Roisenberg, M., dos Santos Nascimento, M., 2021. Deep recurrent neural networks approach to sedimentary facies classification using well logs. IEEE Geoscience and Remote Sensing Letters 19, 1–5.
Fan, X., et al., 2019. Pore structure evaluation of tight reservoirs in the mixed siliciclastic-carbonate sediments using fractal analysis of NMR experiments and logs. Mar. Petrol. Geol. 109, 484–493.
Glover, P.W., 2010. A generalized Archie's law for n phases. Geophysics 75 (6), E247–E265.
Gupta, A.R., Kamal, 2023. A theoretical approach for water saturation estimation in shaly sandstones. Geoenergy Sci. Eng. 228.
Hanai, T., Koizumi, N., Gotoh, R., 1959. Dielectric properties of emulsions: I. Dielectric constants of O/W emulsions. Kolloid Z. 167, 41–43.
He, K., Zhang, X., Ren, S., Sun, J., 2016. Deep residual learning for image recognition. 2016 IEEE Conference on Computer Vision and Pattern Recognition (CVPR), pp. 770–778.
Ho, J., Kalchbrenner, N., Weissenborn, D., Salimans, T., 2019. Axial attention in multidimensional transformers arXiv preprint arXiv: 1912.12180.
Hu, X., et al., 2024. Deep learning algorithm-enabled sediment characterization techniques to determination of water saturation for tight gas carbonate reservoirs in Bohai Bay Basin, China. Sci. Rep-UK 14 (1), 12179.
Jafari Kenari, S.A., Mashohor, S., 2013. Robust committee machine for water saturation prediction. J. Petrol. Sci. Eng. 104, 1–10.
Jiang, S., Zheng, Y., Solomatine, D., 2020. Improving AI system awareness of geoscience knowledge: symbiotic integration of physical approaches and deep learning. Geophys. Res. Lett. 47 (13), e2020GL088229.
Jin, G., Xie, R., Jin, B., 2024. New Insight into data processing of nuclear magnetic resonance logging for pore structure characterization in tight sandstone reservoirs. IEEE Trans. Geosci. Remote. Sens. 62.
Karniadakis, G.E., et al., 2021. Physics-informed machine learning. Nature Reviews Physics 3 (6), 422–440.
Kim, J., Oh, S., Kim, H., Choi, W., 2023. Tutorial on time series prediction using 1D-CNN and BiLSTM: a case example of peak electricity demand and system marginal price prediction. Eng. Appl. Artif. Intell. 126, 106817.
Kuang, L., et al., 2021. Application and development trend of artificial intelligence in petroleum exploration and development. Petrol. Explor. Dev+. 48 (1), 1–14.
Latrach, A., Malki, M.L., Morales, M., Mehana, M., Rabiei, M., 2024. A critical review of physics-informed machine learning applications in subsurface energy systems. Geoenergy Sci. Eng. 239.
Li, P., Liu, M., Alfarraj, M., Tahmasebi, P., Grana, D., 2024. Probabilistic physics-informed neural network for seismic petrophysical inversion. Geophysics 89 (2), M17–M32.
Li, Z., Liu, F., Yang, W., Peng, S., Zhou, J., 2021. A survey of convolutional neural networks: analysis, applications, and prospects. IEEE Trans. Neural. Netw. Learn. Syst. 33 (12), 6999–7019.
Lin, L., Huang, H., Zhang, P., Yan, W., Wei, H., Liu, H., Zhong, Z., 2023. A deep-learning framework for borehole formation properties prediction using heterogeneous well-logging data: a case study of a carbonate reservoir in the Gaoshiti-Moxi area, Sichuan Basin, China. Geophysics 89 (1), WA295–WA308.
Liu, B., Yang, S., Ren, Y., Xu, X., Jiang, P., Chen, Y., 2021a. Deep-learning seismic full-waveform inversion for realistic structural models. Geophysics 86 (1), R31–R44.
Liu, H., Zhao, Y., Luo, Y., Chen, Z., He, S., 2015. Diagenetic facies controls on pore structure and rock electrical parameters in tight gas sandstone. J. Geophys. Eng. 12 (4), 587–600.
Liu, N., et al., 2023. ASHFormer: axial and sliding window based attention with high-resolution transformer for automatic stratigraphic correlation. IEEE Trans. Geosci. Remote. Sens. 61.
Liu, N., et al., 2022a. Seismic data reconstruction via wavelet-based residual deep learning. IEEE Trans. Geosci. Remote. Sens. 60, 1–13.
Liu, Y., Zhang, S., Wang, Z., Zhao, B., Zou, L., 2022b. Global perception network for salient object detection in remote sensing images. IEEE Trans. Geosci. Remote. Sens. 60, 1–12.
Liu, Z., et al., 2021b. Swin transformer: hierarchical vision transformer using shifted windows. Proceedings of the IEEE/CVF International Conference on Computer Vision, pp. 10012–10022.
Lu, C., Wang, Y., Zou, X., Zong, J., Su, Q., 2024. Elastic full-waveform inversion via physics-informed recurrent neural network. IEEE Trans. Geosci. Remote. Sens. 62, 1–16.
Lv, A., Cheng, L., Aghighi, M.A., Masoumi, H., Roshan, H., 2021. A novel workflow based on physics-informed machine learning to determine the permeability profile of fractured coal seams using downhole geophysical logs. Mar. Petrol. Geol. 131.
Mashaba, V., Altermann, W., 2015. Calculation of water saturation in low resistivity gas reservoirs and pay-zones of the Cretaceous Grudja Formation, onshore Mozambique basin. Mar. Petrol. Geol. 67, 249–261.
Miah, M.I., Zendehboudi, S., Ahmed, S., 2020. Log data-driven model and feature ranking for water saturation prediction using machine learning approach. J. Petrol. Sci. Eng. 194, 107291.
Movahhed, A., Bidhendi, M.N., Masihi, M., Emamzadeh, A., 2019. Introducing a method for calculating water saturation in a carbonate gas reservoir. J. Nat. Gas Sci. Eng. 70.
Muller, A.P.O., et al., 2023. Deep pre-trained FWI: where supervised learning meets the physics-informed neural networks. Geophys. J. Int. 235 (1), 119–134.
Oraby, M., 2021. Evaluation of the fluids saturation in a multi-layered heterogeneous carbonate reservoir using the non-archie water saturation model. J. Petrol. Sci. Eng. 201, 108495.
Poupon, A., Leveaux, J., 1971. Evaluation of water saturation in shaly formations. SPWLA Annual Logging Symposium. SPWLA. SPWLA-1971-O.
Raissi, M., Perdikaris, P., Karniadakis, G.E., 2019. Physics-informed neural networks: a deep learning framework for solving forward and inverse problems involving nonlinear partial differential equations. J. Comput. Phys. 378, 686–707.
Ren, Q., et al., 2022. A framework of active learning and semi-supervised learning for lithology identification based on improved naive Bayes. Expert Syst. Appl. 202.
Roques, C., et al., 2020. In situ observation of helium and argon release during fluid-pressure-triggered rock deformation. Sci. Rep. 10 (1), 6949.
Shahin, A., Key, K., Stoffa, P., Tatham, R., 2012. Petro-electric modeling for CSEM reservoir characterization and monitoring. Geophysics 77 (1), E9–E20.
Simandoux, P., 1963. Dielectric measurements on porous media, application to the measurements of water saturation: study of behavior of argillaceous formations. Rev. Inst. Fr. Petrol 18, 93–215.
Song, C., Alkhalifah, T.A., 2022. Wavefield reconstruction inversion via physics-informed neural networks. IEEE Trans. Geosci. Remote. Sens. 60, 1–12.
Su, Y.-L., et al., 2020. A new model for predicting irreducible water saturation in tight gas reservoirs. Pet. Sci. 17, 1087–1100.
Sun, J., et al., 2021. A novel saturation calculation model of fractured-vuggy carbonate reservoir via multiscale pore networks: a case study from Sichuan Basin, China. J. Geophys. Eng. 18 (1), 85–97.
Tatar, A., Yassin, M.R., Rezaee, M., Aghajafari, A.H., Shokrollahi, A., 2014. Applying a robust solution based on expert systems and GA evolutionary algorithm for prognosticating residual gas saturation in water drive gas reservoirs. J. Nat. Gas Sci. Eng. 21, 79–94.
Tian, Y., et al., 2024. A novel deep learning method based on 2-D CNNs and GRUs for permeability prediction of tight sandstone. Geoenergy Sci. Eng. 238.
Wang, H., Wang, M., Chen, S., Hui, G., Pang, Y., 2024a. A novel governing equation for shale gas production prediction via physics-informed neural networks. Expert Syst. Appl. 248.
Wang, L., et al., 2020. Pore structure characteristics of an ultradeep carbonate gas reservoir and their effects on gas storage and percolation capacities in the Deng IV member, Gaoshiti-Moxi Area, Sichuan Basin, SW China. Mar. Petrol. Geol. 111, 44–65.
Wang, Z., et al., 2024b. A review of machine learning applications to geophysical logging inversion of unconventional gas reservoir parameters. Earth Sci. Rev. 258.
Wei, C., Huang, R., Ding, M., Yang, J., Xiong, L., 2022. Characterization of saturation and pressure distribution based on deep learning for a typical carbonate reservoir in the Middle East. J. Petrol. Sci. Eng. 213.
Weinzierl, W., Wiese, B., 2021. Deep learning a poroelastic rock-physics model for pressure and saturation discrimination. Geophysics 86 (1), MR53–MR66.
Wu, J., Yin, X., Xiao, H., 2018. Seeing permeability from images: fast prediction with convolutional neural networks. Sci. Bull. 63 (18), 1215–1222.
Wu, K., Peng, B., Zhai, D., 2024. Boundary-Aware axial attention network for high-quality pavement crack detection. IEEE Trans. Neural Netw. Learn. Syst. 36 (7), 13555–13566.
Xiao, L., Shi, Y., Li, G., Guo, H., Li, J., 2021. A method to predict the resistivity index for tight sandstone reservoirs from nuclear magnetic resonance data. AAPG (Am. Assoc. Pet. Geol.) Bull. 105 (5), 1009–1032.
Xing, L., et al., 2023. Pore-scale modelling on complex-conductivity responses of hydrate-bearing clayey sediments: implications for evaluating hydrate saturation and clay content. Geoenergy science and engineering 221, 211356.
Xiong, F., Ba, J., Gei, D., Carcione, J.M., 2021. Data-Driven design of wave-propagation models for shale-oil reservoirs based on machine learning. J. Geophys. Res. Solid Earth 126 (12).
Xu, J., Xu, L., Qin, Y., 2017. Two effective methods for calculating water saturations in shale-gas reservoirs. Geophysics 82 (3), D187–D197.
Yang, L., Chen, W., Wang, H., Chen, Y., 2021. Deep learning seismic random noise attenuation via improved residual convolutional neural network. IEEE Trans. Geosci. Remote. Sens. 59 (9), 7968–7981.

Yang, L., et al., 2022a. High-Fidelity permeability and porosity prediction using deep learning with the self-attention mechanism. IEEE Trans. Neural. Netw. Learn. Syst. 34 (7), 3429–3443.
Yang, Z., Ma, J., Chen, H., Zhang, J., Chang, Y., 2022b. Context-Aware attentive multilevel feature fusion for named entity recognition. IEEE Trans. Neural. Netw. Learn. Syst. 35 (1), 973–984.
Zhang, B., Xu, J., 2016. Methods for the evaluation of water saturation considering TOC in shale reservoirs. J. Nat. Gas Sci. Eng. 36, 800–810.
Zhang, F., Fan, J., qiu, F., Xie, B., Li, X., Zhang, H., 2022. An enhanced accuracy method to determine oil saturation by carbon/oxygen logging in tight reservoirs. Geophysics 87 (2), D21–D31.
Zhang, G., Liu, J., Xu, K., Jiang, S., Zhang, B., Shi, N., 2024. Characteristics and effectiveness of deep and ultradeep tight sandstone fractures: insights from geologic and geophysical data analysis. Geophysics 89 (5), B383–B399.
Zhang, J., Ambrose, W., Xie, W., 2021. Applying convolutional neural networks to identify lithofacies of large-n cores from the Permian Basin and Gulf of Mexico: the importance of the quantity and quality of training data. Mar. Petrol. Geol. 133.
Zhang, Y., Zhu, X., Gao, J., 2023a. Seismic inversion based on Acoustic wave equations using physics-informed neural network. IEEE Trans. Geosci. Remote. Sens. 61, 1–11.
Zhang, Z., et al., 2023b. A physics-informed convolutional neural network for the simulation and prediction of two-phase Darcy flows in heterogeneous porous media. J. Comput. Phys. 477.
Zhao, H., et al., 2015. Petrophysical characterization of tight oil reservoirs using pressure-controlled porosimetry combined with rate-controlled porosimetry. Fuel 154, 233–242.
Zheng, J., et al., 2023. P-wave prediction method under multi-source spatiotemporal feature fusion and physics-informed neural network. Geoenergy Sci. Eng. 223.
Zheng, W., Zhao, X., Zheng, Y., Pang, Z., 2021a. Nonlocal patch-based fully connected tensor network decomposition for multispectral image inpainting. IEEE Geoscience and Remote Sensing Letters 19, 1–5.
Zheng, W., et al., 2021b. Electrofacies classification of deeply buried carbonate strata using machine learning methods: a case study on ordovician paleokarst reservoirs in Tarim Basin. Mar. Petrol. Geol. 123.
Zhong, Z., Carr, T.R., Wu, X., Wang, G., 2019. Application of a convolutional neural network in permeability prediction: a case study in the Jacksonburg-Stringtown oil field, West Virginia, USA. Geophysics 84 (6), B363–B373.
Zhou, X., et al., 2019. A saturation evaluation method in tight gas sandstones based on diagenetic facies. Mar. Petrol. Geol. 107, 310–325.
Zhu, B., Ren, S., Weng, Q., Si, F., 2024. A physics-informed neural network that considers monotonic relationships for predicting NOx emissions from coal-fired boilers. Fuel 364, 131026.